frontiers | Frontiers in Cell and Developmental Biology

TYPE Original Research
PUBLISHED 30 May 2023
DOI 10.3389/fcell.2023.1195037

Check for updates

OPEN ACCESS

EDITED BY
Dmitri S. Kudryashov,
The Ohio State University, United States

REVIEWED BY
Agnes Hackl,
University Hospital of Cologne, Germany
Hani Y. Suleiman,
Washington University in St. Louis, United States

*CORRESPONDENCE
Lori L. O'Brien,
lori_obrien@med.unc.edu

RECEIVED 27 March 2023
ACCEPTED 03 May 2023
PUBLISHED 30 May 2023

CITATION
Gerlach GF, Imseis ZH, Cooper SL, Santos AN and O'Brien LL (2023), Mapping of the podocin proximity-dependent proteome reveals novel components of the kidney podocyte foot process.
Front. Cell Dev. Biol. 11:1195037.
doi: 10.3389/fcell.2023.1195037

COPYRIGHT
© 2023 Gerlach, Imseis, Cooper, Santos and O'Brien. This is an open-access article distributed under the terms of the Creative Commons Attribution License (CC BY). The use, distribution or reproduction in other forums is permitted, provided the original author(s) and the copyright owner(s) are credited and that the original publication in this journal is cited, in accordance with accepted academic practice. No use, distribution or reproduction is permitted which does not comply with these terms.

Mapping of the podocin proximity-dependent proteome reveals novel components of the kidney podocyte foot process

Gary F. Gerlach, Zachary H. Imseis, Shamus L. Cooper, Anabella N. Santos and Lori L. O'Brien*

Department of Cell Biology and Physiology, University of North Carolina at Chapel Hill, Chapel Hill, NC, United States

Introduction: The unique architecture of glomerular podocytes is integral to kidney filtration. Interdigitating foot processes extend from the podocyte cell body, wrap around fenestrated capillaries, and form specialized junctional complexes termed slit diaphragms to create a molecular sieve. However, the full complement of proteins which maintain foot process integrity, and how this localized proteome changes with disease, remain to be elucidated.

Methods: Proximity-dependent biotin identification (BioID) enables the identification of spatially localized proteomes. To this end, we developed a novel *in vivo* BioID knock-in mouse model. We utilized the slit diaphragm protein podocin (*Nphs2*) to create a podocin–BioID fusion. Podocin–BioID localizes to the slit diaphragm, and biotin injection leads to podocyte-specific protein biotinylation. We isolated the biotinylated proteins and performed mass spectrometry to identify proximal interactors.

Results and Discussion: Gene ontology analysis of 54 proteins specifically enriched in our podocin–BioID sample revealed 'cell junctions,' 'actin binding,' and 'cytoskeleton organization' as top terms. Known foot process components were identified, and we further uncovered two novel proteins: the tricellular junctional protein Ildr2 and the CDC42 and N-WASP interactor Fnbp1l. We confirmed that Ildr2 and Fnbp1l are expressed by podocytes and partially colocalize with podocin. Finally, we investigated how this proteome changes with age and uncovered a significant increase in Ildr2. This was confirmed by immunofluorescence on human kidney samples and suggests altered junctional composition may preserve podocyte integrity. Together, these assays have led to new insights into podocyte biology and support the efficacy of utilizing BioID *in vivo* to interrogate spatially localized proteomes in health, aging, and disease.

KEYWORDS

podocyte, BioID proximity labeling, foot process, aging, Ildr2, Fnbp1l, cell junction, slit diaphragm

Introduction

The kidneys perform vital functions as they filter waste and toxins from the blood and regulate body fluid homeostasis. The simplest functional unit of the kidney is the nephron, composed of a blood filter, termed the glomerulus, connected to a segmented tubule. The glomerulus operates as a 'molecular sieve,' filtering blood and inhibiting the passage of large macromolecules and red blood cells into the nephron tubule. The glomerulus relies on specialized epithelial cells called podocytes, named for their unique cellular morphology with long extruding projections, termed foot processes. Podocyte foot processes wrap around a tuft of fenestrated endothelial capillaries leaving small gaps, or slits, between them. Podocytes undergo morphological changes to their junctional architecture during development to form a specialized barrier between foot processes, termed a slit diaphragm (Reeves et al., 1978; Quaggin and Kreidberg, 2008; Ichimura et al., 2015). The slit diaphragm executes multiple functions, including macromolecular filtering, in collaboration with the underlying glomerular basement membrane; connection to the actin cytoskeleton to maintain foot process architecture; and signaling that regulates podocyte integrity. The slit diaphragm is distinct from other junctional complexes as it integrates unique structural components and components of adherens and tight junctions (Kestilä et al., 1998; Boute et al., 2000; Reiser et al., 2000; Donoviel et al., 2001; Fukasawa et al., 2009). Nearly 50 years ago, a zipper-like model for the slit diaphragm was proposed, wherein proteins from the neighboring foot processes partially cross the intervening intercellular space and overlap, forming the dense protein-rich slit diaphragm structure eloquently visualized by electron microscopy (EM) (Rodewald and Karnovsky, 1974; Karnovsky and Ryan, 1975). The more recent block-face scanning EM revealed a 'ridge-like prominence' architecture to podocyte foot processes, formed on the basal surface of the primary foot process (Ichimura et al., 2015; Miyaki et al., 2020). These investigations underscore the continued advancement in our understanding of podocyte structure and function.

When podocytes undergo stress or injury above a threshold, they initiate a response that leads to foot process effacement, loss of slit diaphragms, and proteinuria. Loss of podocyte integrity, observed as effacement, is associated with proteinuric kidney disease (Pagtalunan et al., 1997; van den berg et al., 2004; D'Agati, 2003). This pathology has been described in both acquired and hereditary forms of glomerular disorders or podocytopathies (Kopp et al., 2020). Podocytopathies are a class of kidney diseases in which direct or indirect podocyte injury drives proteinuria or nephrotic syndrome and can ultimately lead to end-stage renal disease (ESRD). Genetic studies have previously identified mutations in numerous podocyte foot process components, such as membrane-associated guanylate kinase WW and PDZ domain containing 2 (MAGI2) (Bierzynska et al., 2017), CD2-associated protein (CD2AP) (Gigante et al., 2009; Liu et al., 2021), nephrin (NPHS1) (Kestilä et al., 1998; Beltcheva et al., 2001), and podocin (NPHS2) (Boute et al., 2000; Guaragna et al., 2015), as causal for nephrotic disease. Additionally, diseases such as diabetes and autoimmune disorders can lead to podocyte injury (Lu et al., 2019). While the downstream result is effacement and loss of slit diaphragms, we know little about the temporal changes occurring specifically within the foot process and locally at the slit diaphragm.

Identification of slit diaphragm protein complexes with immunoprecipitation followed by mass spectrometry (MS) has uncovered important localized interactions (Pierchala et al., 2010; Kocylowski et al., 2022). However, the efficiency of these immunoprecipitations is often hindered by harsh conditions required to extract membrane proteins, which can eliminate weaker binding interactions, or by antibodies that may disrupt interactions. Additionally, transient interactions may be missed in such experiments. Podocin is known to localize to the slit diaphragm and interacts with Nphs1 (nephrin), Neph1 (Kirrel), and Cd2ap (Huber et al., 2001; Schwarz et al., 2001; Roselli et al., 2002; Sellin et al., 2003). Podocin is a member of the stomatin family, containing a central hinge region that integrates into the membrane of the foot process with cytoplasmic N- and C-termini (Schurek et al., 2014). Previous studies demonstrated podocin's role in the development of the multiprotein–lipid super complex of the slit diaphragm (Schwarz et al., 2001). Podocin's ability to oligomerize and act as a protein scaffold at slit diaphragms ideally positions it for use as a bait protein in proteomic studies.

The discovery and engineering of a promiscuous prokaryotic biotin ligase by Roux and colleagues and concomitant development of omics technologies in the last decade have laid the groundwork to uncover spatially localized proteomes (Roux et al., 2012; Kim et al., 2016). Proximity-dependent biotin identification, or BioID, utilizes a mutated prokaryotic biotin ligase fused to a bait protein of interest to covalently attach biotin to proteins within the vicinity of the bait protein. The radius of biotinylation can range from ~10 nm to 25 nm, dependent on the size of the linker between the bait and the biotin ligase, allowing for biotinylation of both direct and indirect interactors (Roux et al., 2012; Kim et al., 2016). The BioID system requires exogenous addition of biotin for the ligase to covalently biotinylate a proximally located protein, giving the BioID system spatiotemporal control of protein tagging. Additionally, the biotin labels are stable and can withstand harsh isolation conditions, allowing the capture of transient interactors and membrane proteins. The BioID system has provided plentiful *in vitro* reports from cell culture models that highlight the power of the system and its ability to discover novel components of even well-documented cellular machinery, such as the centrosome and cilium (Firat-Karalar et al., 2014; Mick et al., 2015). There have been limited *in vivo* reports of BioID, but it has been used successfully in vertebrates such as zebrafish and mice to identify endogenous interactomes (Firat-Karalar et al., 2014; Uezu et al., 2016; Rudolph et al., 2020). To the best of our knowledge, this approach has not been employed in the mammalian kidney.

Here, we utilized gene editing to introduce a smaller, more efficient promiscuous biotin ligase (BioID2) (Kim et al., 2016) into the endogenous murine *Nphs2* locus to create a fusion protein, hereafter referred to as podocin–BioID (*Nphs2*^{BioID2}). Our podocin–BioID model has the ability to uncover proteins that localize to the region of the podocyte foot process within the vicinity of podocin in an *in vivo* mammalian system. We were able to identify novel podocyte foot process proteins and furthermore how this proteome changes with age, highlighting the utility of our model for uncovering new interactors and disease-associated changes.

Results

Generation of the *Nphs2*^{BioID2} knock-in mouse model

To generate our mouse model, we utilized CRISPR/Cas9 gene editing in combination with homology-directed repair to knock-in

10.3389/fcell.2023.1195037

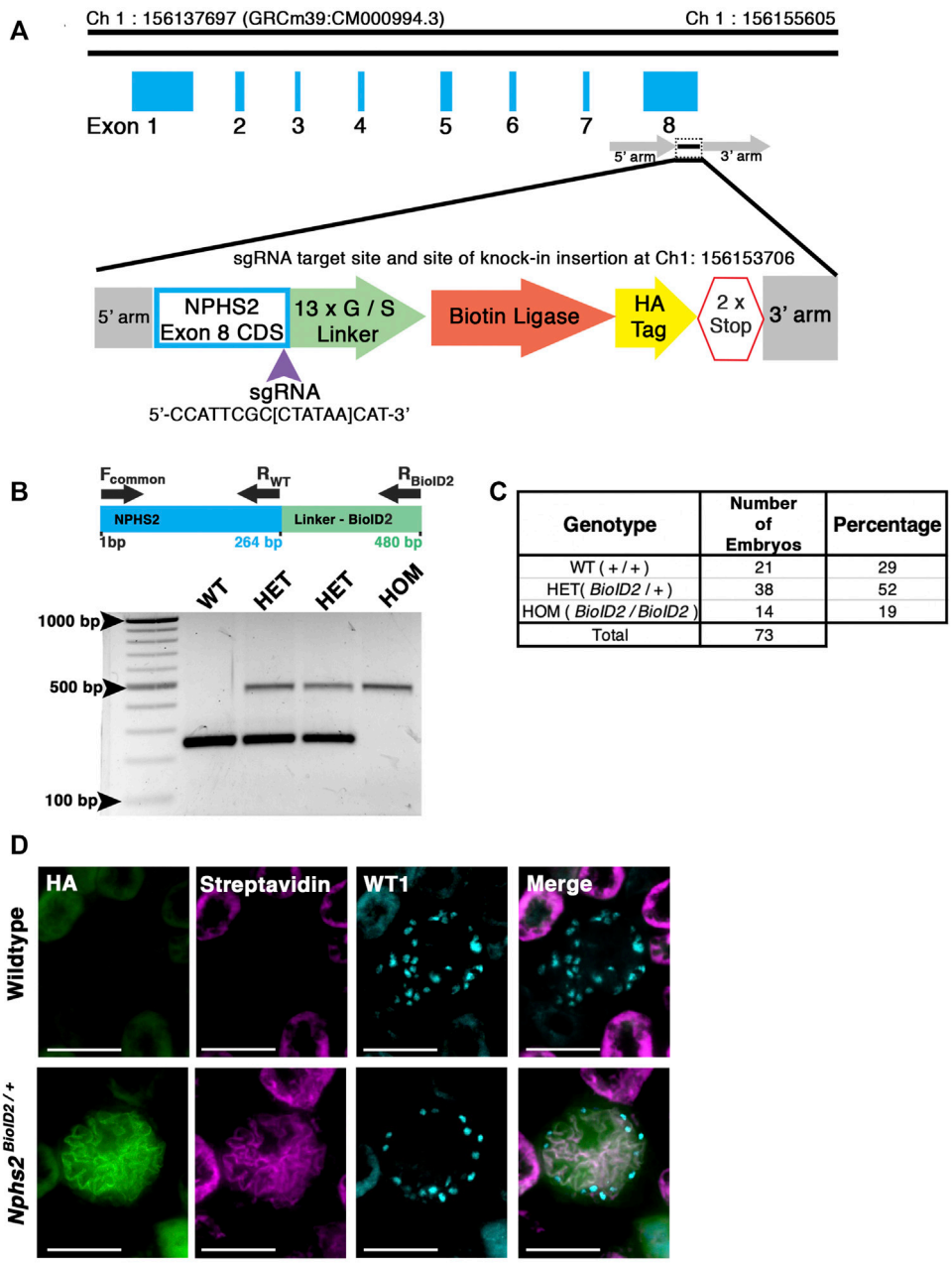

FIGURE 1
Generation of a knock-in *Nphs2*^{BioID2} mouse line via CRISPR/Cas9 genome editing of the *Nphs2* locus. **(A)** Schematic of the CRISPR/Cas9 genome editing strategy utilized to generate the *Nphs2*^{BioID2} mouse line. A small guide RNA (sgRNA), targeting the stop codon in exon 8 of *Nphs2* (purple arrowhead), was combined with a donor vector containing the knock-in cassette (zoom view) to induce homologous recombination and integrate the BioID2 moiety containing a 13x glycine/serine (G/S) linker, biotin ligase, and HA tag into the *Nphs2* locus. **(B)** Genotyping strategy (top panel). Wild-type (a single band at 264 base pairs (bp)), heterozygous (two bands; one at wild-type size of 264 bp and a second that amplifies the BioID2 linker region giving a band at 480 bp), or homozygous (a single band at the 480 bp). **(C)** Genotyping of 73 embryos at E18.5-P0 verifies a relative Mendelian ratio of genotypes being recovered (25:50:25). **(D)** Immunofluorescence analysis of 8–10-week-old adult mice injected with biotin shows an enrichment of streptavidin within the glomerulus of *Nphs2*^{BioID2} mice and absence of streptavidin signal in control littermate mice. The HA signal from the BioID2 moiety closely overlaps with that of streptavidin (merged image). Wt1 (cyan) is utilized as a podocyte marker to delineate the glomerular boundaries. Scale bar: 50 μm.

the HA-tagged, mutated *A. aeolicus* biotin ligase (BioID2) in frame at the *Nphs2* locus (Kim et al., 2016). A single guide RNA (sgRNA) was used to target the stop codon within the eighth exon of *Nphs2* to create the fusion. A 13x glycine/serine(G/S) flexible linker region was included between *Nphs2* and the ligase to provide up to a 25-nm reach (Figure 1A) (Kim et al., 2016). C57BL/6J zygotes were injected, and after screening the resulting animals for a single knock-in with the correct sequence, several founders were identified. A single male

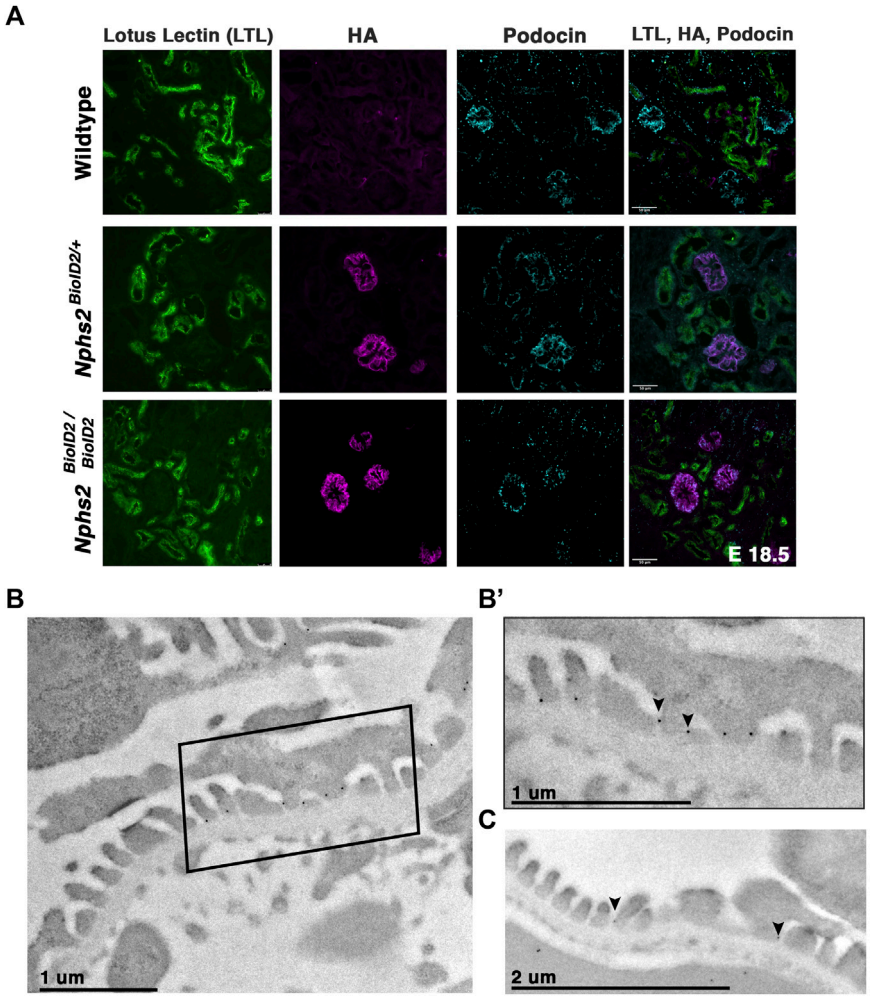

FIGURE 2
Nphs2^{BioID2} animals present normal kidney morphology with podocin–BioID localized to podocytes, and specifically the slit diaphragm. **(A)** E18.5 littermates of wild-type, heterozygous (*Nphs2*$^{BioID2/+}$), and homozygous (*Nphs2*$^{BioID2/BioID2}$) animals were analyzed for gross nephron morphology and localization of podocin–BioID. Proximal tubule: (LTL, green); BioID: (HA, magenta); podocytes/glomerulus: (podocin, cyan). Scale bar: 50 μm **(B)** Transmission electron microscopy (TEM) and immunogold labeling of the HA (BioID) of 4-week-old *Nphs2*$^{BioID2/+}$ kidneys. Boxed area is shown in **(B')**. **(B')** Magnified view of the boxed region from the panel **(B)**. The HA signal localizes as dark spherical dots from immunogold labeling (arrowheads). Scale bar: 1 μm **(C)** Wildtype littermates immunogold-labeled for podocin (arrowheads). Scale bar: 2 μm.

founder was utilized for subsequent breeding and expansion of the *Nphs2*^{BioID2} line. Genotyping E18.5-P0 pups from incrosses of *Nphs2*$^{BioID2/+}$ animals identified wildtype, heterozygous, and homozygous offspring at approximately anticipated Mendelian ratios of 29%, 52%, and 19%, respectively (n = 73, Figures 1B, C). However, we were typically unable to recover homozygous *Nphs2*$^{BioID2/BioID2}$ pups after 1 week of birth. Overall, the gross morphology of homozygous pups and kidneys appeared normal at P0, and we were unable to determine the specific cause of their death. We speculate that altered podocin function associated with *Nphs2* expression in other tissues, such as the craniofacial region, may cause phenotypes like nursing defects in homozygous *Nphs2*$^{BioID2/BioID2}$ pups (Supplementary Figure S1A) (Diez-Roux et al., 2011). Due to the early death of homozygous animals, all subsequent experiments for proteomic profiling were performed on heterozygous *Nphs2*$^{BioID2/+}$ animals. To test the function of podocin–BioID fusion and determine if the ligase could biotinylate podocyte proteins, we administered 5 mg/kg biotin for 7 consecutive days to 8–10-week-old *Nphs2*$^{BioID2/+}$ and wild-type control mice, a dosage utilized in previous protocols for *in vivo* BioID experiments (Uezu et al., 2016). Following 1 week of subcutaneous biotin injections, the kidneys harvested from *Nphs2*$^{BioID2/+}$ mice displayed a pronounced streptavidin signal within glomeruli and specifically podocytes marked by Wt1-positive nuclei (Figure 1D). We occasionally detected a streptavidin-positive signal within the tubules, which either represents background staining or uptake of free biotin, as controls also displayed this non-glomerular signal pattern. Finally, probing for the HA tag contained within the podocin–BioID fusion shows that the HA signal overlaps with the streptavidin signal, confirming that the fusion protein is being specifically translated in podocytes and that the biotin ligase is functional (Figure 1D).

Podocin–BioID kidneys display normal nephron morphology and the fusion protein localizes to the slit diaphragm

We next sought to confirm that the kidneys of animals expressing the podocin–BioID fusion did not display any significant phenotypic differences, most specifically to the nephron. If the fusion protein was not localizing or functioning properly, the animals may display phenotypes associated with *Nphs2* knockout animals such as enlarged glomeruli, vacuolated podocytes, and mesangial expansion (Roselli et al., 2004). Additionally, dilated tubules may indicate abnormal nephron function. Immunostaining kidney sections of wild-type, heterozygous, and homozygous animals at E18.5 revealed no qualitative differences in glomerular size or proximal tubule dilation (Figure 2A). This further supports that mislocalization or abnormal function of podocin–BioID in podocytes is not the likely cause of death in homozygous animals. Additionally, $Nphs2^{BioID2/+}$ animals did not present significant increase of protein in their urine (proteinuria), which would be indicative of compromised podocyte function (Supplementary Figure S1B). Immunofluorescence staining showed a significant overlap between the HA signal and the signal from a podocin-specific antibody, evincing that the fusion protein is localizing properly in heterozygous animals and that it is being expressed at similar levels in homozygous animals (Figure 2A). Importantly, we did not observe the HA antibody signal anywhere besides the glomerulus.

Additionally, we wanted to verify that the podocin–BioID protein localized to the slit diaphragm where podocin is known to interact with other slit diaphragm proteins and play a functional role (Huber et al., 2001; Schwarz et al., 2001; Roselli et al., 2002; Sellin et al., 2003; Roselli et al., 2004). We utilized immunogold labeling in combination with transmission EM (TEM) to examine the subcellular localization of the podocin–BioID protein (Figures 2B, B'; Supplementary Figure S2). $Nphs2^{BioID2+}$ kidney sections were stained with an anti-HA antibody, followed by a colloidal Gold-AffiniPure secondary antibody. Punctate gold signals were observed near electron-dense regions between foot processes, the location of the slit diaphragm (Figures 2B, B' arrowheads) (Supplementary Figure S2B, arrowheads). We observed minimal gold signals outside of this region, suggesting restriction of podocin–BioID protein to the foot process (Supplementary Figures S2A, B). To confirm that this is the site of normal podocin localization in our control animals, wild-type littermates were probed with a podocin antibody and also showed localization of punctate gold signals near the electron-dense region of the slit diaphragm (Figure 2C, arrowheads).

An enrichment of biotinylated proteins is detected in lysates from $Nphs2^{BioID2/+}$ kidneys

To enrich our podocin–BioID protein lysates for glomeruli, we surgically isolated the cortex from each kidney of biotin-injected $Nphs2^{BioID2/+}$ animals and wild-type controls at 8–10 weeks. Isolated cortices were homogenized and lysed to obtain protein lysates from each animal. Protein lysates were applied to magnetic streptavidin-coated beads to isolate the biotinylated proteins, and an aliquot was removed and tested to validate the efficacy of the biotin ligase. By Western blot analysis, we identified an increase in the number of biotinylated proteins in our $Nphs2^{BioID2/+}$ sample *versus* wild-type along the full spectrum of molecular weights (Figure 3A). In contrast, few streptavidin-labeled, biotinylated, proteins were visible in controls (Figure 3A). The few biotinylated proteins observed in wild-type littermates likely represent the endogenous metabolic CoA carboxylases (Sears et al., 2019). Due to podocin's ability to oligomerize and the heterozygous nature of the mice, we expect that endogenous, non-tagged podocin would be biotinylated, as well as podocin-BioID. When we probed for podocin using Western blot, we observed two bands within the $Nphs2^{BioID2/+}$ sample: one band at approximately 50 kDa, the predicted endogenous podocin molecular weight without the BioID2 tag (Figure 3C, denoted with an asterisk), and a second larger protein, podocin–BioID (Figure 3C, denoted with arrowhead). No bands for podocin or podocin–BioID were detected in controls, as expected. Additionally, the HA signal on the BioID2 protein was only detected in our $Nphs2^{BioID2/+}$ protein lysates, confirming the purity and specificity of our results (Figure 3B). We then tested if biotin could cross the placental barrier to be delivered to embryonic pups via injection of the pregnant dam. Pregnant dams were injected each day for 1 week, from E11.5–E18.5, subcutaneously with 5 mg/kg biotin. Pups were then collected at P0. We analyzed the kidney cortex and observed a strong streptavidin signal within the glomeruli of P0, $Nphs2^{BioID2/+}$ mice (Figure 3D, arrowheads). On the contrary, we did not observe any signal in wild-type control littermate mice. Collectively, these data highlight the efficacy and specificity of our podocin–BioID model, which can be utilized across a spectrum of ages.

Identification of the podocyte foot process proteome by mass spectrometry profiling

Kidney cortices of three 8- to 10-week-old, sex-matched mice were collected as one biological replicate, after biotin administration for 1 week. All MS analyses were run in triplicate, *i.e.,* nine mice per condition, totaling 18 mice ($Nphs2^{BioID2/+}$ *vs.* control littermates) per MS analysis (Supplementary Table S1). To representatively capture the podocyte foot process proteome, we combined the results of three separate MS analyses (Figure 4; Supplementary Table S1). Significant sex differences were not apparent in our studies (Supplementary Tables S2–S5). From our proteomics analysis, 11 proteins were found across all three MS analyses to have an averaged $\log_2$ fold change ≥2.5. Many of these top-ranking proteins including podocin, Kirrel, Tjp1, Pard3b, Magi2, Dnd, and Synpo are found to localize to the slit diaphragm (Asanuma et al., 2007). Yet, others including an immunoglobulin-like domain containing receptor 2 (Ildr2) and a formin-binding protein 1 like (Fnbp1l, also known as Toca1) were, until now, unreported components of the podocyte foot process. Additionally, six proteins were identified across two MS analyses as significantly enriched with an average $\log_2$ fold change ≥1.75. These include documented slit diaphragm components Tjp2 and Cd2ap (Figure 4A). All top 17 proteins had a stringent $\log_2$ fold change ≥1.75. The list of significant foot process proteins identified from each MS analysis is reported in

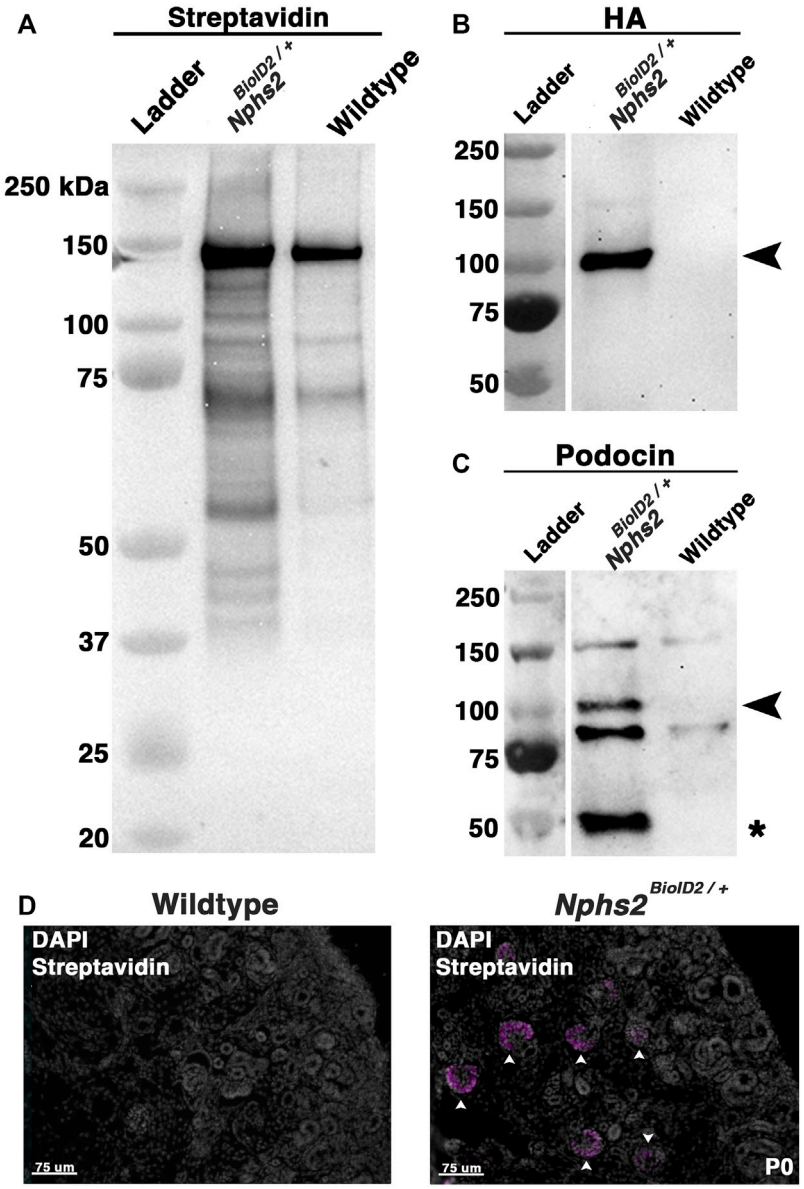

FIGURE 3
Biotin-administered *Nphs2*$^{BioID2/+}$ mice show an enrichment of biotinylated proteins specifically within the glomeruli. **(A)** Lysates from biotin-injected *Nphs2*$^{BioID2/+}$ and wild-type age-matched 8–10-week-old littermate controls were subjected to protein separation, Western blot, and probed for streptavidin. **(B)** Streptavidin isolates blotted with an anti-HA antibody exhibit robust and specific detection of the HA signal only within the *Nphs2*$^{BioID2/+}$ sample (arrowhead). **(C)** Streptavidin isolates probed for podocin show two specific bands for both BioID2-tagged podocin (arrowhead) and endogenous podocin (asterisk). **(D)** Micrographs of P0 kidney sections showing DAPI (gray) and streptavidin (magenta) labeling. Pregnant dams were injected with 5 mg/kg of biotin from E11.5 to E18.5. Arrowheads show glomeruli labeled with streptavidin. Scale bar: 75 μm.

Supplementary Tables S2–S5. To add support to our relative $\log_2$ fold cut off, we assayed an immunoglobulin superfamily adhesion molecule, Jam1/F11r, (Ebnet et al., 2004) with an observed $\log_2$ fold expression change of 0.7 (Supplementary Table S3). We identified Jam1 expression in cells of the proximal convoluted tubule, abutting the glomerulus, (Supplementary Figure S3) but not within the glomerulus. Potentially, non-glomerular cortex proteins that are biotinylated are also isolated, although these appear minimal in our findings. However, this helped establish a relative cutoff for fold-change for which we identify non-podocyte proteins.

To surmount a complete list of podocyte foot process proteins, we established a $\log_2$ fold change cutoff at 1.2 across all three MS analyses and excluded histone, ribosome, and mitochondrial proteins to have a catalog of 54 proteins (Supplementary Table S5). A volcano plot graphically depicting the compiled proteome with a total of ~1,400 proteins identified and cataloging proteins with a $\log_2$ fold change ≥1.75 and adjusted p-value ≤ 0.05, which are represented by green dots, with proteins found to have an adjusted p-value ≤ 0.05 represented by blue dots and proteins not found to be significant represented by grey dots is given in Figure 4B;

10.3389/fcell.2023.1195037

A

Gene Symbol	Protein Names	*p*-Value	Log_2 Fold Change
Kirrel	Kin of IRRE-like protein 1	0.0006	7.75
Tjp1	Tight junction protein ZO-1	0.002	7.63
Nphs2	Podocin	0.019	6.70
Pard3b	Partitioning defective 3 homolog B	0.008	6.39
Magi2	Membrane-associated guanylate kinase, WW and PDZ domain-containing protein 2	0.018	6.29
Cttn	Src substrate cortactin	0.001	5.60
Ddn	Dendrin	0.003	5.56
Nebl	LIM zinc-binding domain-containing Nebulette	0.010	4.93
Ildr2	Immunoglobulin-like domain-containing receptor 2	0.007	4.90
Fnbp1l	Formin-binding protein 1-like	0.014	4.27
Synpo	Synaptopodin	0.047	2.90
Tjp2	Tight junction protein ZO-2	0.014	4.71
Myzap	Myocardial zonula adherens protein	0.009	3.45
Cd2ap	CD2-associated protein	0.020	3.18
Col1a1	Collagen alpha-1(I) chain	0.007	2.05
Aif1l	Allograft inflammatory factor 1-like	0.014	1.86
Tns2	Tensin-2	0.022	1.75

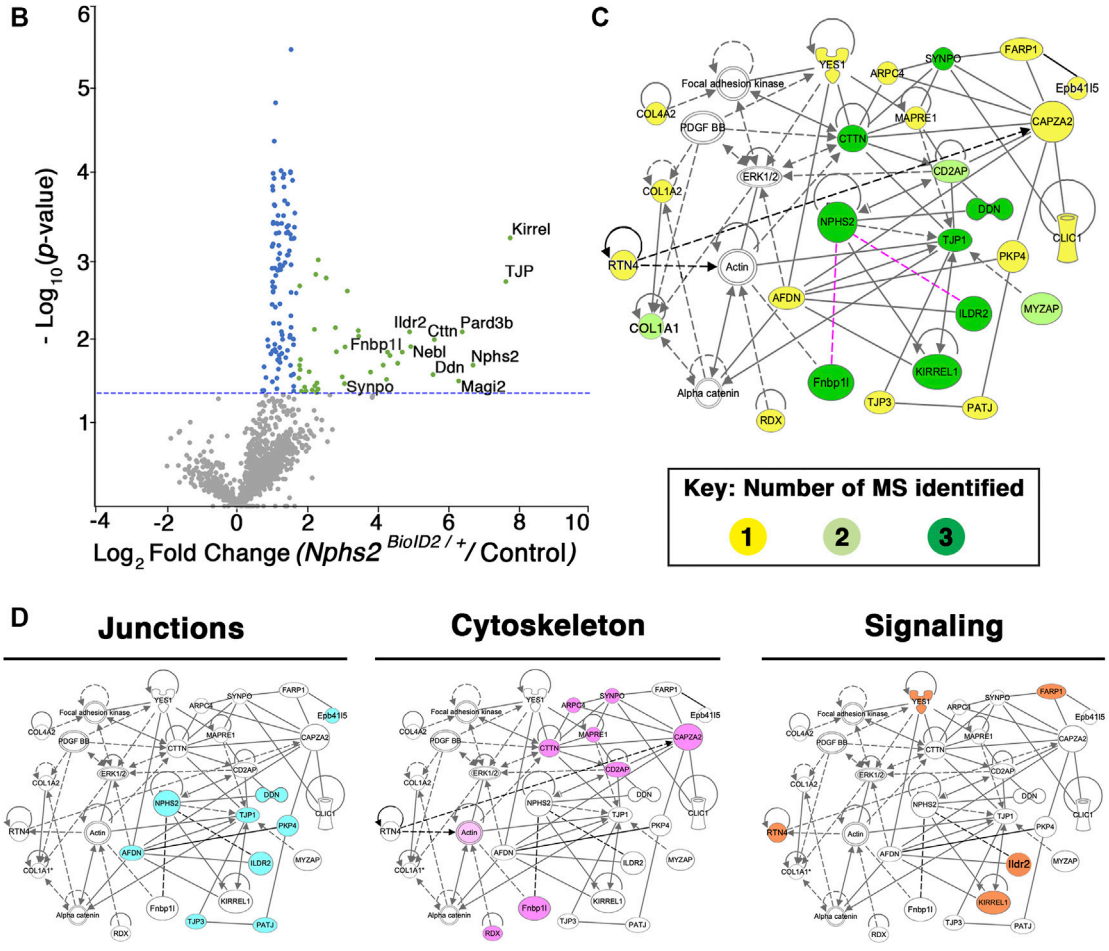

FIGURE 4
Proteomics profiling of the podocyte foot process identifies documented slit diaphragm components and novel candidates with unexplored podocyte function. **(A)** Three separate MS analyses were combined, and the average log_2 fold change and respective adjusted *p*-values were averaged to produce a list of the top foot process proteins. The top 11 proteins were identified across all three MS profiles. Six additional proteins were identified across two of the three MS analyses, denoted following the thick black bar. **(B)** A volcano plot depicting approximately 1,400 proteins identified across all three MS analyses. Green dots represent the 40 proteins identified across three separate MS profiles as having a log_2 fold change ≥1.7, and *p*-value ≤ 0.05, blue dots denote all proteins identified to have a significant *p*-value ≤ 0.05, and gray dots are proteins with a *p*-value ≥ 0.05. The top 11 proteins consistently uncovered across all MS analyses are embedded with gene symbols in the plot. The blue dotted line represents a *p*-value ≤ 0.05. **(C)** Network topology was generated utilizing *Qiagen Ingenuity Pathway Analysis* (IPA) on the top 54 proteins from our cumulative proteomic profiles. IPA produces a proposed web of relationships from published literature, with most of our top proteins represented, (11 of 17), with documented connections to other foot

(*Continued*)

FIGURE 4 (Continued)
processes and slit diaphragm components. The color intensities of each protein (yellow to green) represent the number of MS analyses from which each protein was identified. Darker green shade = all three MS analyses, lighter green shade = two of three MS analyses, and yellow = a single MS analysis. Dotted lines and unshaded proteins represent predicted interactions/interactors from IPA, respectively. Magenta lines are novel proteins identified in this study to be present within the podocyte foot process. **(D)** Dissecting the IPA network identifies three central nodes representing proteins associated with junctions (cyan), cytoskeleton (magenta), and signaling (orange).

A

Gene Ontology (GO) Category	Cluster	Enrichment Score	Counts	*p*-Value
Molecular Function (MF)	Cytoskeletal Protein Binding	4.53	12	2.20×10^{-7}
	Actin Binding		6	7.80×10^{-5}
Cellular Component (CC)	Cell-Cell Junction	4.42	12	7.70×10^{-8}
	Adherens Junction		10	7.90×10^{-6}
Biological Process (BP)	Cytoskeleton Organization	2.61	14	3.20×10^{-7}
	Actin Filament-Based Process		12	8.70×10^{-8}

B

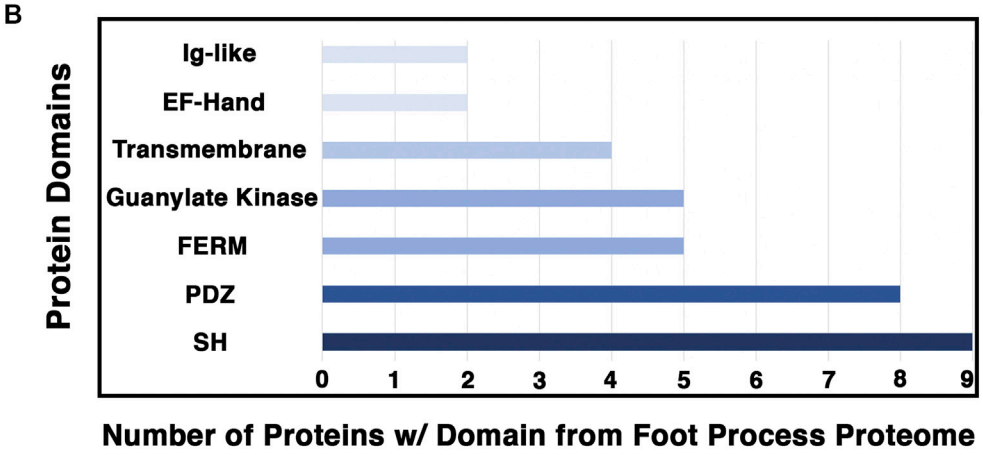

FIGURE 5
Analysis of the podocyte foot process proteome identifies the cytoskeleton, cell–cell junctions, and actin-based processes as the top GO categories with respective protein domains that align with these functions. The Database for Annotation, Visualization, and Integrative Discovery (DAVID) was utilized for GO clustering analysis of the top 54 proteins identified to have a $\log_2$ fold change ≥1.20, and *p*-value ≤ 0.05 (Supplementary Table S5). **(A)** Overlap in GO readout was observed across the three separate GO categories analyzed, molecular function, cellular component, and biological process, with cytoskeleton, actin, and cellular junctions being the top hits. The respective top clusters within each GO category are listed, alongside the relative enrichment score, number of proteins, and *p*-values. **(B)** Protein domain analysis of the top 54 podocyte foot process proteins provides evidence for protein–protein interactions and likely scaffold and protein–protein complex formation. Each protein's respective protein domains were binary-counted for presence or absence within the proteomics profile. The top seven protein domains identified from the podocyte foot process proteome consist of a Src homology (SH) (*n* = 9 proteins), PSD-95, disc large, and ZO—1 (PDZ) (*n* = 8), 4.1 protein, Ezrin, Radixin and Moesin (FERM) (*n* = 5), guanylate kinase (*n* = 5), transmembrane (*n* = 4), E and F helix–Hand (EF–Hand) (*n* = 2), and an immunoglobulin-like (Ig–like) domain (*n* = 2). Cumulatively, these seven domains represent ~50% of the top proteins identified from the foot process proteome (26/54).

Supplementary Table S5. The blue dotted line represents a $-\log_{10}$ (*p*-value ≤ 0.05) (Figure 4B). All significantly identified proteins ($p \leq 0.05$) had at least two unique peptides identified via MS analysis. The most highly detected and significant proteins from our proteomic profiling, clustering with documented slit diaphragm components, are found in the right scatter of the volcano plot, depicted with green dots (Figure 4B; Supplementary Table S5).

To analyze our proteomic findings further, the top 54 podocyte foot process proteins were utilized for *in silico* analyses. We input Supplementary Table S5 into *Qiagen Ingenuity Pathway Analysis* (IPA) and performed a variant effect analysis to compute a proposed interactome based on published literature (Figure 4C). The representative web of interactions from IPA was color-coded based on the number of MS analyses each protein appeared in, one (yellow), two (light green), and three (dark green) (Figure 4C). Two novel foot process proteins were identified by IPA, Ildr2 and Fnbp1l, to be involved in the interactome with connections to afadin and actin, respectively (Figure 4C). We added two dotted magenta lines for potential interactions of Ildr2 and Fnbp1l with podocin (Figure 4C). Unshaded proteins and dashed lines are predicted interactors/interactions from IPA. Our IPA-proposed network includes 26 of our 54 input foot process proteins. The IPA

10.3389/fcell.2023.1195037

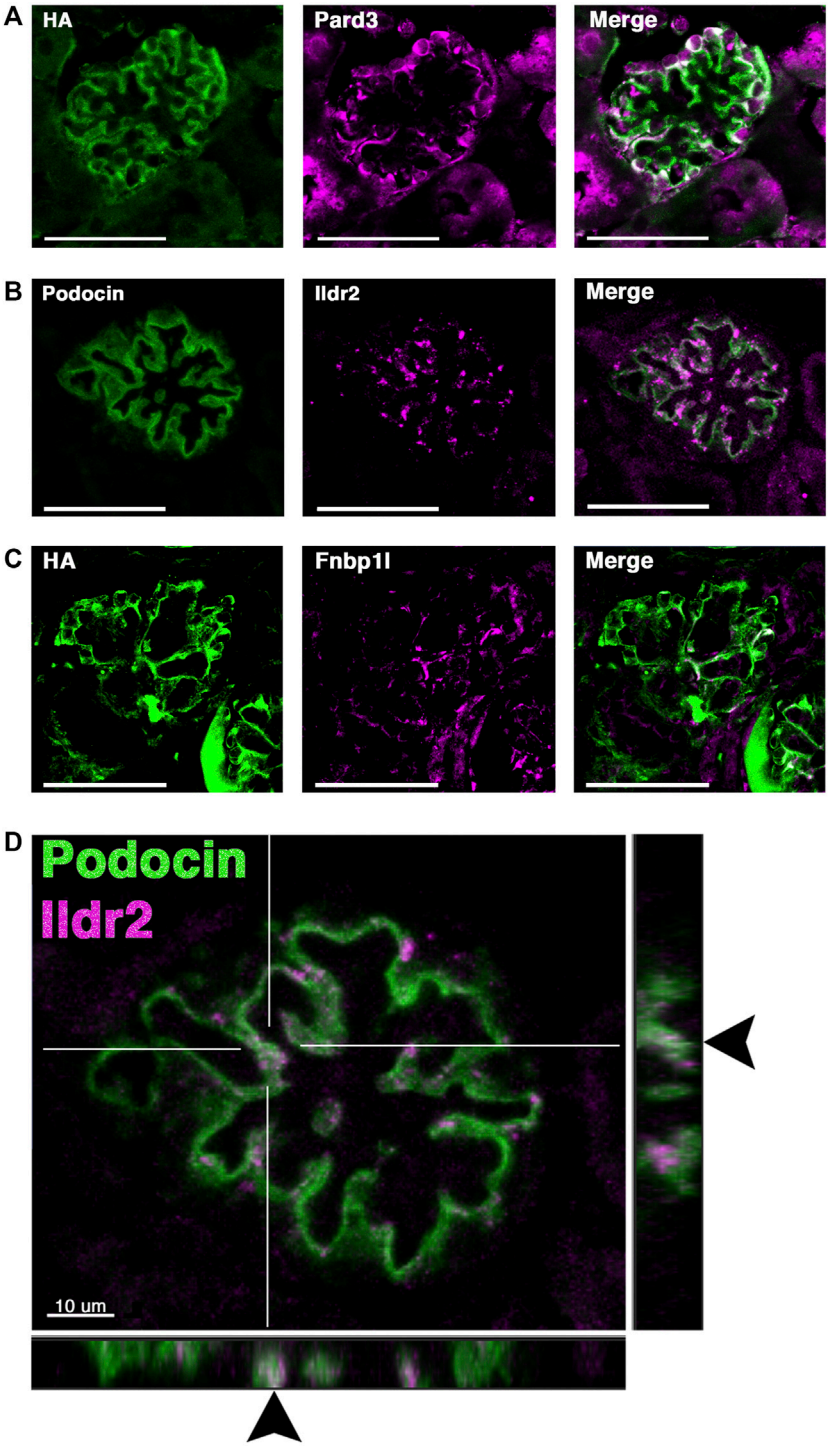

FIGURE 6
Two novel foot process candidates, Ildr2 and Fnbp1l, localize to podocytes and overlap with podocin. **(A)** Micrographs showing Pard3 (magenta) localization within podocytes and colocalization with the HA signal of podocin–BioID (green). **(B)** Co-immunostaining of Ildr2 (magenta) and podocin (green) within the glomerulus. **(C)** Fnbp1l (magenta) colocalization with the HA signal of podocin–BioID (green) in the glomeruli. Scale bars in **(A–C)**: 50 µm **(D)** A merged image of podocin (green) and Ildr2 (magenta) through a confocal z-projection shows punctate localization of Ildr2 and overlap (arrowheads) with podocin in the z-plane in the left and bottom panels. Scale bar in **(D)**: 10 µm.

interactome identifies three main nodes, *i.e.*, junctions, cytoskeleton, and signaling (Figure 4D). We highlighted the respective proteins that contribute to each node for junctions (cyan), cytoskeleton (magenta), and signaling (orange) (Figure 4D). We then input these 54 proteins into the *Database for Annotation, Visualization, and Integrated Discovery (DAVID)* to identify the Gene Ontogeny

(GO) terms that are most highly enriched across our foot process proteome. DAVID analysis identified cytoskeleton protein binding, cell–cell junctions, and actin filament-based processes as the top molecular function, cellular component, and biological processes GO terms, respectively (Figure 5A). Additionally, DAVID and IPA overlap in their representation of junctional signaling and actin binding as top GO terms and the canonical pathway, respectively. Taken together, these findings align with the major functional roles of podocin and other foot process/slit diaphragm components.

To further decipher the contributions of our top 54 podocyte foot process proteins to junctions and cell–cell contacts, we cataloged the protein domains represented within each protein. We utilized binary counting for the presence and absence of a domain. We did not account for the number of same/similar domain(s), *i.e.*, SH2/3, within a protein. We identified seven top protein domains within the catalog of the podocyte foot process proteome that included SH, PDZ, FERM, and Ig-like domains, among others (Figure 5B). All of these top protein domains align with the nodes of the podocyte foot process proteome, *i.e.*, junctions, cytoskeleton, and signaling.

Ildr2 and Fnbp1l are expressed by podocytes and co-localized with podocin

Our proteomic analyses uncovered several proteins which have not been previously described to localize to the podocyte foot process or have podocyte-specific functions. We, therefore, validated their expression in podocytes and any colocalization with podocin. We utilized immunofluorescence on kidney sections to visualize the location of three proteins in particular: Myozap, Fnbp1l, and Ildr2. First, a known slit diaphragm and foot process component which was identified in our proteomics, Pard3b, was assessed for its colocalization with podocin. Pard3b exhibited positive staining in the glomerulus and overlapped with the HA signal of podocin–BioID (Figure 6A). Pard3b positive staining is also found in the adjacent tubule cells, where it helps maintain epithelial integrity (Figure 6A) (Gerlach and Wingert, 2014). Myozap regulates cardiac function through Rho-dependent activity and interacts with junctional proteins such as ZO-1 (Seeger et al., 2010). It was identified across two of the three MS analyses (Figure 4A), and therefore we decided to investigate its localization. Utilizing an antibody against a synthetic human MYOZAP peptide, (Pieperhoff et al., 2012), we identified a strong signal of Myozap in the kidney endothelium, both in the glomerular capillaries and outside of glomerular structures (Supplementary Figure S4). Myozap exhibits some degree of overlap with podocin; however, the majority of Myozap protein detection does not colocalize with podocin, suggestive of additional roles outside of podocytes (Supplementary Figure S4).

We identified Fnbp1l, a documented junctional and actin-organizing protein, (Ho et al., 2004; Van Itallie et al., 2015) across all three MS analyses, with a $\log_2$ fold change >4 (Figure 4). Fnbp1l has been identified in human and mouse podocytes from single-cell RNA-seq analysis and linked to podocyte cytoskeleton dynamics *in vitro*, although it has not been documented to colocalize with the slit diaphragm or foot process-associated proteins (Lu et al., 2017; Wu et al., 2018). We found that Fnbp1l co-localizes with podocin in continuous stretches within the glomeruli observed as a white signal from the Fnbp1l (magenta) and podocin (green) overlap (Figure 6C). *In situ* hybridization confirms the glomerular expression of *Fnpb1l* (Supplementary Figure S5C' arrowhead), similar to *Nphs2* (Supplementary Figure S5A), in addition to a tubular expression pattern at postnatal day 2 (P2).

Ildr2, a member of the B7 superfamily of immunoglobulins, is found highly enriched in the podocyte foot process proteome across all MS profiles, with an average $\log_2$ fold change of 4.9 (Figure 4). Ildr2 has pivotal roles in immunomodulation and maintenance of peripheral self-tolerance, evincing immunomodulatory activity and the ability to ameliorate autoimmune disease states in various mouse models (Hecht et al., 2018; Podojil et al., 2018; Huetter et al., 2020). Ildr2 is also a member of the angulin family and localizes to tricellular junctions of *in vitro* cultured epithelial cells (Higashi et al., 2013). In the kidney, Ildr2 exhibited a punctate staining pattern that colocalized with podocin in adult mouse glomeruli, reminiscent of the punctate and restricted pattern of tricellular junction staining observed *in vitro* (Figures 6B, D arrowheads) (Higashi et al., 2013). In the z dimension, we observe the overlap of Ildr2 (magenta) with podocin (green) as white punctate foci denoted by arrowheads (Figure 6D). We further validated *Ildr2* expression within the glomeruli via *in situ* hybridization. *Ildr2* expression is observed in the glomeruli (Supplementary Figure S5B', arrowhead) and renal tubule cells (Supplementary Figure S5B', arrow) in P2 mice. We verified Ildr2 localization within early renal vesicles, comma, and S-shaped bodies of developing nephrons at E15.5 (Figure 7B; Supplementary Figure S6). Ildr2 is more membranous and contiguous, yet with some punctate detection at E15.5, both within podocytes and cells of the developing nephron tubule (Figure 7B). Collectively, these studies provide evidence that Ildr2 and Fnbp1l are novel podocyte foot process components that likely help maintain podocyte architecture.

Ildr2 protein levels increase in both mouse and human glomeruli with age

To determine whether our podocin–BioID model can detect changes to the localized proteome due to aging, we performed proteomics on ~2-year-old (108 weeks) male $Nphs2^{BioID2/+}$ mice and compared the results to those observed in our 8–10-week-old $Nphs2^{BioID2/+}$ male mice to assess the changes to the proteome (Figure 7A). We identified significant increases in Tjp2 and Pkp4 and the largest change (2.76-fold) in Ildr2. We were unable to detect any significant decrease in proteins at $p \leq 0.05$, although Fnbp1l and Tns2 showed a decreasing trend. We observed minimal change in podocin when comparing the two age groups (Figure 7A). To assess the relevance of our findings in humans, we assayed ILDR2 immunofluorescent staining in kidney sections of young (age ~30 years) and aged (91-year-old) humans. ILDR2 displayed a similar punctate staining pattern in glomeruli of young humans. In correlation with our findings from the mouse, we found an increase in ILDR2 staining in the aged glomeruli. Interestingly, the expression pattern no longer displays a punctate pattern, but rather a more diffuse membranous staining pattern, similar to the mouse E15.5 stage (Figures 7B, C). To verify the specificity of the increased

10.3389/fcell.2023.1195037

A

Gene Symbol	Protein Names	BioID (Young) vs WT Log_2 Fold Change	BioID (Aged) vs WT Log_2 Fold Change	*p*-Value
Ildr2	Immunoglobulin-like domain-containing receptor 2	2.76	3.53	0.001
Tjp2	Tight junction protein ZO-2	2.71	3.31	0.01
Pkp4	Plakophilin-4	2.27	2.94	0.01
Nphs2	Podocin	2.42	2.36	0.10
Fnbp1l	Formin-binding protein 1-like	3.22	2.12	0.10
Tns2	Tensin-2	1.30	0.36	0.10

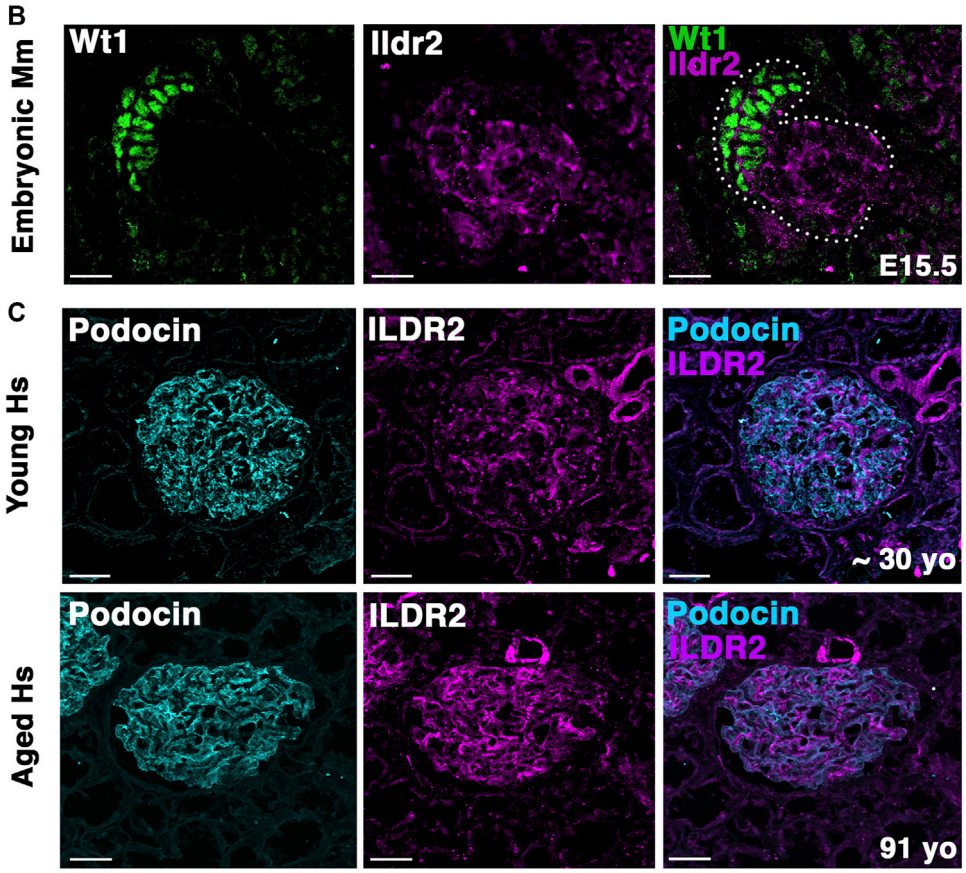

FIGURE 7
Ildr2 is detected in developing nephron structures and shows increased signal in glomeruli of aged mice and humans compared to that in the glomeruli of young mice and humans. **(A)** Proteomic profiling of two aged (~2 years; 108 week old) male *Nphs2*$^{BioID2/+}$ mice compared to 8–10 week-old *Nphs2*$^{BioID2/+}$ mice. Table lists three significantly increased proteins, podocin, and two decreased proteins. All proteins were detected with at least two razor unique peptides. **(B)** Micrographs of E15.5 kidney sections showing Ildr2 (magenta) in developing nephron structures (dotted outline) of mice (Mm; *Mus musculus*) with podocytes denoted by the Wt1 (green). Scale bar: 20 µm. **(C)** Micrographs of sections from young (~30-year-old) and aged (91-year-old) human (Hs; *Homo sapiens*) kidneys tissue coimmunostained for ILDR2 (magenta) and podocin (cyan). Scale bar: 50 µm.

ILDR2 signal to podocytes, we coimmunostained kidney sections with ITGA8 (mesangial marker) and CD31 (endothelial marker) (Supplementary Figure S7) and found minimal overlap of ILDR2 with either ITGA8 or CD31 and the most significant overlap of signal with podocin, albeit more diffuse (Figure 7C; Supplementary Figure S7). We quantified the corrected total glomerular fluorescence (CTGF) by selecting the glomerulus as a region of interest (gROI) and then quantifying the total fluorescence intensity and subtracting out the mean background fluorescence for the glomerular area, *i.e.*, total gROI fluorescence—(glomerular area x mean background fluorescence) = CTGF, (Figure 8). We confirmed a significant ($p \leq 0.007$) increase in ILDR2 in aged human glomeruli compared to young human kidney tissues (Figure 8), thus validating the ability of our podocin–BioID mouse model to detect conserved changes in proteomes with aging.

Discussion

Podocytes are extraordinary epithelial cells of the kidney that intertwine their foot process extensions to establish a cellular junction, the slit diaphragm, which is distinct from other cellular junctions in the human body. The slit diaphragm was identified more than 5 decades ago as an electron-dense region between two podocyte foot processes, as visualized by EM (Rodewald and

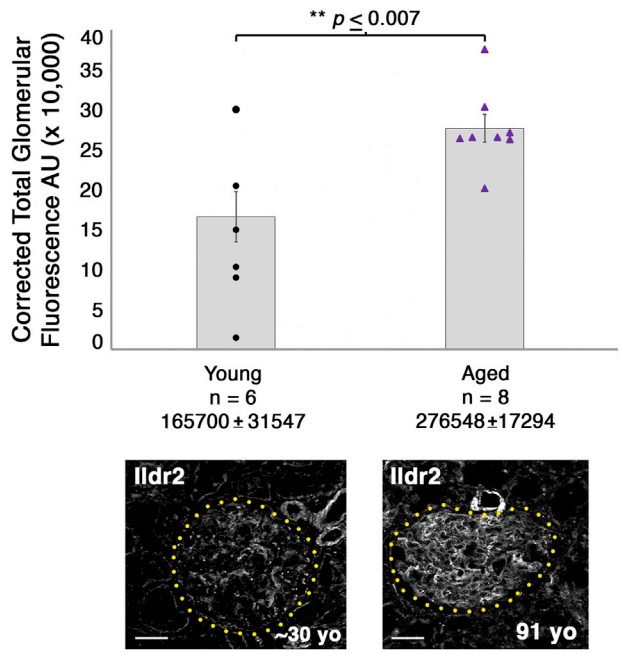

FIGURE 8
Glomeruli of aged humans exhibit a significant increase in ILDR2 corrected total glomerular fluorescence (CTGF) compared to the glomeruli of young humans. ILDR2 CTGF was calculated by selecting the glomeruli as the ROI and then measuring the total fluorescence within the area and subtracting out the sum of the area by the average background fluorescence, *i.e.*, total gROI fluorescence—(area of glomerulus *x* mean of background fluorescence) = CTGF. Two examples of glomeruli are shown from each age and outlined in yellow dots to depict the respective ROI utilized to calculate the CTGF. Scale bar: 50 μm.

Karnovsky, 1974; Karnovsky and Ryan, 1975). Many proteins that compose the slit diaphragm when mutated are associated with nephrotic diseases, including nephrin, podocin, Magi2, and Cd2ap (Kopp et al., 2020). Loss of podocyte integrity is one of the most common clinical observations in kidney disease. ESRD, being one among the top 10 causes of death in the US, necessitates the need to identify novel components of the slit diaphragm, and how the slit diaphragm changes with disease, to help spur the development of new therapeutic options and identify biomarkers of disease severity.

We utilized a new *in vivo* biochemical tool to interrogate the proteome of the podocyte foot process via knock-in of a BioID moiety, generating our podocin–BioID model. The sensitivity and advantage of BioID is that it allows for weak and transient interactions to be identified, in addition to withstanding harsh isolation conditions (Kestilä et al., 1998). Furthermore, the biotin–streptavidin interaction is one of the strongest known non-covalent interactions, enhancing the isolation of biotinylated proteins via a streptavidin-coated magnetic bead. We validated our model recapitulates normal podocin localization by TEM and shows that podocin-BioID localizes to the slit diaphragm. Activity of the biotin ligase was confirmed through probing kidney sections and lysates with streptavidin and finding an enrichment of biotinylated proteins. Our proteomics profiling identified more than 50 candidate molecules with significant enrichment in the podocyte foot process, $\log_2 \geq 1.2$. Within this dataset, we identified protein interactors known to associate with podocin as well as novel candidates not found in previous investigations of the slit diaphragm and the podocin-associated proteome (Pierchala et al., 2010; Kocylowski et al., 2022). Additionally, we identified changes to the localized proteome that occur with aging. It would be interesting to compare the proteome across additional stages, such as during development. Podocytes begin as a columnar epithelium with only tight and adherens junctions which remodel and later mature to form the specialized slit diaphragm complex (Bierzynska et al., 2017). With the ability of biotin to cross the placental barrier, the proteome could be compared from development to maturity to identify changes that explain how these specialized junctions are formed.

The proteomics analysis revealed potential nuances of the podocyte foot process that are still under investigation. We identified 11 proteins that are repeated over all three MS profiles. However, there were more than 30 proteins that only surfaced in a single MS analysis and split across the three MS analyses. While this may be due to experimental variability, such as in the isolation of proteins, this may also highlight some differences in biological activity in the foot process. The dynamics, variability, and protein turnover in the podocyte slit diaphragm are relatively unknown. Pointing to the variability of one documented component, synaptopodin (Synpo), across the three MS analyses, the respective $\log_2$ fold changes were observed at 1.0, 2.9, and 4.8, which indicates potential protein turnover, variability in the slit diaphragm components, or potential variability of MS detection. Furthermore, a second documented slit diaphragm protein, Cd2ap, was only identified in two of the MS profiles. These cofounding issues made a single MS analysis provide a limited view, or snapshot, of the proteins present within the podocyte foot process. By combining three separate MS analyses, we uncovered a more complete profile of the podocyte foot process and slit diaphragm. Many of the top candidates identified in the podocyte foot process proteome are well-documented slit diaphragm components including Kirrel, Nphs2, Par3, Magi1/2, Tjp1/2/3, Dnd, Synpo, and Cd2ap. Furthermore, our *in silico* analysis utilizing DAVID highlights anticipated GO terms, including actin binding, cell–cell junctions, adherens junctions, and cytoskeleton organization that align with podocyte function. We conclude the podocin–BioID model provides a spatial-specific approach to identify proteins that are notoriously difficult to isolate.

We cannot rule out that biotin delivery, metabolism, and selective labeling may limit some proteins from being detected. One report depicts a time lapse of biotin administration *in vivo* with positive streptavidin enrichment for as long as 18 h after biotin administration (Branon et al., 2018; May et al., 2020). However, biotin requires an accessible primary amine within a peptide to biotinylate. Proteins with little open structures or a limited number of lysine residues could be missed by the labeling strategy. The possibility that proteins were missed is brought to light by the inability to identify nephrin (*Nphs1*) across any of the MS analyses run. One rationale for the inability to identify nephrin, a known slit diaphragm molecule that interacts with podocin, posits that its C-terminal domain is only minimally accessible to podocin, while the remaining majority of the 180 kDa protein spans the

extracellular space of the slit diaphragm (Schwarz et al., 2001). Therefore, while there are significant advantages to the BioID system over traditional immunoprecipitations followed by MS, it is also subject to missing important interactions. Additionally, we did not identify a significant enrichment of solute transporters as in a recent MS analysis of the podocin-associated proteome (Kocylowski et al., 2022). This may represent a more restricted localization of the modified podocin–BioID protein along the foot process, the inability to biotinylate these proteins, or the lack of enrichment in our studies due to their normal biotinylation without the addition of excess biotin. Altogether, these findings highlight the efficacy of using or combining multiple approaches to obtain a more complete understanding of the localized proteome.

One of the novel foot process candidates we identified, Fnbp1l, has multiple roles in microtubule binding, cell polarity, motility, actin organization, junctional localization, and signaling (Ho et al., 2004; Van Itallie et al., 2015). Based on these roles, we hypothesize that Fnbp1l similarly helps maintain the slit diaphragm and foot process integrity through association with the actin cytoskeleton and links to the slit diaphragm. Single-cell RNA-seq analyses have previously found *Fnbp1l* expression in human (Wu et al., 2018) and mouse podocytes and tubule cells (Lu et al., 2017), and MS has identified it in whole podocyte analyses (Boerries et al., 2013; Rinschen et al., 2018). As observed from the Kidney Interactive Transcriptomics (KIT), *Fnbp1l* is most highly expressed in podocytes compared to the human renal tubule cells (Wu et al., 2018). Furthermore, *Fnbp1l* is also expressed in the zebrafish pronephros (Thisse and Thisse, 2004), with a similar pattern to other zebrafish tight junction proteins such as ZO-1/2 (McKee et al., 2014). However, the specific expression of *Fnbp1l* within the zebrafish podocytes remains unknown. With the conservation of *Fnbp1l* expression in the renal system across vertebrates, it likely plays an important role in helping maintain epithelial integrity in various cells of the nephron, including podocytes.

Ildr2/ILDR2 is found to be specifically expressed in mouse and human podocytes as observed from publicly available databases including KIT (Wu et al., 2018; Wu et al., 2019), and MS identified it in proteomic analyses of whole podocytes (Rinschen et al., 2018). *Ildr2* was also identified as a Wt1 transcriptional target in podocytes by ChIP-seq (Ettou et al., 2020). However, none of these studies noted the expression of Ildr2 or interrogated its localization within the kidney or podocytes. We found that in early embryonic and postnatal mouse kidneys, *Ildr2*/Ildr2 is expressed and localized to tubule cells and podocytes. However, in the adult kidney, Ildr2 localization becomes restricted to podocytes. During podocyte development, we observe a more membranous and contiguous pattern of Ildr2 in comma and S-shaped bodies, with some foci of heightened detection. In mature glomeruli, Ildr2 is restricted to punctate foci that colocalize with podocin. We postulate that podocyte epithelial junctional complexes, which change during development as podocytes acquire their unique architecture, alter its localization pattern (Ichimura et al., 2017). Ildr2 has been identified at the site of tricellular tight junctions (tTJs) in the murine retinal pigment epithelium and *in vitro* within EpH4, a mouse mammary gland cell line (Higashi et al., 2013; Hecht et al., 2018). Additionally, Ildr2 has recently been identified to interact with afadin in human embryonic kidney cells (HEK293) (Go et al., 2021). Afadin is also reported to localize to the site of specialized tricellular junctions and mediate mechanotransduction (Yu and Zallen, 2020). Although we did not detect the enrichment of other tTJ components in our MS analyses, the relative abundance of Ildr2 over other proteins or its spatial orientation may have enabled its specific detection. The role of mechanical strain present from the underlying fluid flow shear stress on these specialized tTJs and recruitment of specific proteins to these domains remains unresolved. The function and even the localization of tTJs in podocytes are poorly understood. Many proteins identified in the podocyte foot process proteome are documented junctional proteins containing classified SH, PDZ, FERM, transmembrane, EF-hand, and Ig-like domains. Yet, Ig-like domain-containing proteins were a considerably smaller population. It is intriguing to speculate that Ig-like domains or a combination of PDZ, SH, and Ig-like domains aids in the recruitment of specific proteins to specialized junctions such as tTJs and the slit diaphragm. Furthermore, the requirement of these proteins for managing stress, such as from changes in fluid flow from the fenestrated endothelium and conversely the potential requirement of mechanostress for recruitment of proteins to these tTJs and slit diaphragms, needs further investigation.

In our aged podocin–BioID mice and our aged human kidney sample, we identified an increase in Ildr2 within podocytes. The pattern of Ildr2 is more membranous with some punctate foci in embryonic renal structures, yet becomes detectable only as punctate foci as the mouse matures. Proteomic profiling of kidneys from ~2-year-old mice showed a significant enrichment and increase of Ildr2 *v*ersus 8–10-week-old mouse kidneys. We validated that ILDR2 significantly increases in aged (91-year-old) human glomeruli via quantifying the corrected total glomerular fluorescence of glomeruli in young and aged humans. We further noted that in the aged human glomeruli, the ILDR2 signal is more abundant in zones where the podocin signal is less, and conversely where the podocin signal is high, the ILDR2 signal is less abundant, although there is still overlap between the two proteins. The ILDR2 signal appears to be specific to podocytes, as minimal overlap of the ILDR2 signal was detected with mesangial (ITGA8) and endothelial (CD31) markers. Aged human glomeruli present an ILDR2 pattern that more closely resembles the mouse embryonic stage, with a contiguous pattern rather than the punctate pattern of 8–10-week-old mice. The expression of podocyte junctional components has been shown to change with age (Wang et al., 2020). We hypothesize that increasing Ildr2/ILDR2 protein in aged podocytes helps maintain podocyte integrity. This likely allows podocytes to withstand physiological changes that occur with aging through the modification of junctional components. The additional increase of tight junction and desmosome-associated proteins Tjp2 and Pkp4, respectively, in our aged mouse proteome further supports this hypothesis.

In this study, we developed an innovative tool for identification of novel proteins within a spatially restricted podocyte foot process/slit diaphragm. Current efforts are now aimed at uncovering proteins differentially regulated during slit diaphragm development, aging, and in renal disease. It is crucial we uncover the changing composition of the podocyte slit diaphragm and foot process as it holds potential for new therapeutic treatment targets to either preserve or prevent the loss of podocyte integrity in kidney disease.

Materials and methods

Genetic CRISPR/Cas9 engineering of the Nphs2 locus to append a BioID2 moiety

CRISPR/Cas9 targeting and donor vector design were performed by UNC Chapel Hill Animal Models Core. *Benchling* software was used to identify Cas9 single guide RNAs (sgRNA) overlapping the podocin (*Nphs2*) stop codon. Guide RNAs were cloned into a T7 promoter vector followed by *in vitro* transcription and spin column purification. Functional testing was performed by transfecting a mouse embryonic fibroblast cell line with sgRNA and Cas9 protein (produced and purified by the UNC Protein Expression Core). The sgRNA target region was amplified from transfected cells and analyzed by T7 endonuclease 1 assay (New England Biolabs). sgRNA, *Nphs2*-g78B (protospacer sequence 5′-gCCATTCGCCTATAACAT-3'; lower case g indicates heterologous guanine added at the 5′ end of the native sequence for efficient T7 *in vitro* transcription) was selected for genome editing in embryos. *Nphs2* was amplified from adult mouse kidney cDNA and cloned into the MCS-13X Linker-BioID2-HA plasmid (MCS-13x Linker-BioID2-HA was a gift from Kyle Roux (Addgene plasmid # 80899; http://n2t.net/addgene:80899; RRID:Addgene_80899) (Kim et al., 2016). A donor vector was subsequently constructed from the *Nphs2*-13x Linker-BioID2-HA plasmid with the following features: 1) a 1,018 bp 5′ homology arm encompassing the sequence immediately 5′ of the *Nphs2* stop codon including a 276-bp coding sequence from *Nphs2* exon 8; 2) a 267-bp in-frame glycine-/serine-rich linker sequence, 3) a 696-bp coding sequence for the humanized biotin ligase of *A. aeolicus* with a R40G mutation in the catalytic domain (BioID2) (Kim et al., 2016); 4) HA tag; 5) a 2X stop codon; 6) a FRT site, and 7) a 1,019-bp 3′ homology arm, beginning at the *Nphs2*-sgRNA cut site. The donor vector was designed to produce a final knock-in allele, which would produce a fusion protein of podocin C-terminally linked to BioID2.

Embryo microinjection

C57BL/6J zygotes were microinjected with 400 nM Cas9 protein, 25 ng/μL sgRNA, 20 ng/μL supercoiled double-stranded donor plasmid (Mix1) or 200 nM Cas9 protein, 12.5 ng/μL sgRNA, and 10 ng/μL donor plasmid (Mix2). Injected embryos were implanted in pseudopregnant B6D2F1 recipient females. Sixteen resulting pups (nine from Mix1 and seven from Mix2) were screened by PCR for the presence of the knock-in allele. One female (Founder #2) and one male (Founder #6) were positive for the correct single-copy knock-in allele. Founders #2 and #6 were mated to wild-type C57BL/6J animals for transmission of the knock-in allele. Both founders transmitted the correct knock-in allele to offspring. Injections, genotyping of founders, and off-site targeting analysis were performed by UNC Chapel Hill Animal Models Core.

Genotyping

A mouse tail or ear clip was taken and dissociated with Viagen DirectPCR Lysis Reagent (Mouse Tail) containing 10 μg/mL proteinase K incubated at 55°C overnight and denatured at 95°C for 10 min. PCR was run with ($T_{annealing}$ = 63.5°C), with an elongation time of 40 s, for 35 cycles. Primer sequences utilized for genotyping are common Forward: 5′-CTTTTGTCCTCTCCCGGCAA-3′, podocin WT Reverse 5′-TGCATGTAGCCATCTTGTGACT-3′, *Nphs2*^{BioID2} Reverse 5′-CTGCCCTTGGTCTGTCTGTC-3'.

Kidney cortex isolation and lysis

Mice were raised, housed, and handled in accordance with the IACUC protocol number 19-183.0/22-136.0. Mice (8–10-week-old) were injected subcutaneously with 5 mg/kg biotin every day for 1 week. We surgically isolated the cortex of the kidney to enrich for the glomerular fraction, using a scalpel in cold sterile phosphate-buffered saline (PBS). A single biological sample was composed of the isolated kidney cortex of three same-sex mice for a total of six kidney cortexes per sample (two kidneys per animal × three mice) (Supplementary Table S1). The sample was then homogenized via a glass Dounce homogenizer. The samples were centrifuged at 4°C, 5000 × g for 10 min. The supernatant was decanted, and the tissue pellets snap-frozen in liquid nitrogen and stored at −80°C. Care was taken to utilize sterile Eppendorf tubes that had not been autoclaved as we identified a contaminant (polyethylene glycol) in a preliminary MS analysis that may arise from autoclaving the plastic utilized. The samples were removed from the freezer and allowed to equilibrate on ice for 2 h. Lysis buffer (8 M urea, 50 mM Tris-HCl pH 7.4, 500 mM NaCl, 2.5 mM EDTA, 2.5 mM EGTA, 1.5 mM $MgCl_2$, 1.5 mM DTT, 0.25% NP-40, 1% SDS, and 1x protease inhibitors (Roche cOmplete Mini EDTA-free, Sigma)) was then added to resuspend the pellet and allowed to nutate at 4°C for 1 hour. The protein homogenate was sonicated (three pulses for 10 s at a duty cycle of 30%) and centrifuged (4°C, 12,000 rpm for 10 min). The supernatant was then removed for subsequent quantification and analysis.

Biotinylated protein capture

Kidney cortex-isolated protein lysates were serially diluted and run in triplicate on a 96-well plate reader at 590 nm wavelength (Synergy HT, BioTek). A standard curve of bovine serum albumin (BSA) was utilized as a control. Protein concentrations of each lysate were calculated, and 10 mg of crude protein lysate was loaded with 100 μL of streptavidin-coated magnetic beads (Dynabeads MyOne Streptavidin C1, Invitrogen). Samples containing beads and protein lysate were rotated end-over-end at 4°C overnight. The supernatant was removed using a magnetic strip, and the bead-captured fraction was washed once with lysis buffer. After the first wash with the lysis buffer containing 1% SDS and 0.25% NP-40, decreasing amounts of detergents were utilized in subsequent washes until there was no detergent remaining in the wash buffer (after four washes). Beads were then washed three times in ABC solution (50 mM ammonium bicarbonate, 8.0 pH) and sent to UNC Chapel Hill Hooker Proteomics Core. All procedures were performed in the same manner for our cohort of aged mice, with the exception that 5 mg of crude protein lysate was loaded onto the beads.

After the last wash buffer step, 50 µL of 50 mM ammonium bicarbonate (pH 8) containing 1 µg trypsin (Promega) was added to beads overnight at 37°C with shaking. The next day, 500 ng of trypsin was added and then incubated for an additional 3 h at 37°C with shaking. Supernatants from pelleted beads were transferred, and then beads were washed twice with 50 ul LC/MS-grade water. These rinses were combined with the original supernatant and then acidified to 2% formic acid. Peptides were desalted with peptide desalting spin columns (Thermo Scientific) and dried via vacuum centrifugation. Peptide samples were stored at −80°C until further analysis.

LC/MS/MS analysis

Each sample was analyzed by LC-MS/MS using an Easy-nLC 1200 coupled to a QExactive HF (Thermo Scientific). The samples were injected onto an EASY-Spray PepMap C18 column (75 µm id × 25 cm, 2 µm particle size) (Thermo Scientific) and separated over a 120-min method. The gradient for separation consisted of a step gradient from 5% to 36–48% mobile phase B at a 250 nL/min flow rate, where mobile phase A was 0.1% formic acid in water and mobile phase B was 0.1% formic acid in ACN. The QExactive HF was operated in data-dependent mode, where the 15 most intense precursors were selected for subsequent HCD fragmentation. Resolution for the precursor scan (m/z 350–1700) was set to 60,000 with a target value of 3×10^6 ions, 100 ms inject time. MS/MS scan resolution was set to 15,000 with a target value of 1×10^5 ions, 75 ms inject time. The normalized collision energy was set to 27% for HCD, with an isolation window of 1.6 m/z. Peptide match was set to preferred value, and precursors with unknown charge or a charge state of 1 and ≥8 were excluded. The MS data have been deposited to the ProteomeXchange Consortium (http://www.proteomexchange.org/) via the PRIDE partner repository (https://www.ebi.ac.uk/pride/) with the dataset identifier PXD042302.

Western blot

Biotinylated proteins attached to streptavidin-coated bead were eluted off with excess biotin [200 mM] in 200 mM Tris HCl pH: 6.8, 40% glycerol, 8% beta mercaptoethanol, 2% SDS, and 0.04% bromophenol blue at 95°C for 30 min. Bead slurry mix was placed on a magnet, and isolated biotinylated lysate was collected for subsequent analysis. Protein sample fractions were removed and loaded into a Novex WedgeWell gel (4–20% Tris-Glycine gradient gel, Invitrogen, XP04202), and run in 25 mM Tris-HCl, 190 mM glycine, 0.1% SDS, and pH 8.3. Proteins were transferred from gel to a nitrocellulose membrane in 25 mM Tris-HCl, 190 mM glycine, and 20% methanol. The membrane was blocked in 3% bovine serum albumin in 1x TBST (Tris-buffered Saline Solution (25 mM Tris-HCl pH 7.5, 150 mM NaCl) with 0.1% Tween-20, for 1 h at room temperature. Primary antibodies (Rabbit anti-HA tag (Cell Signaling, 3724S [1:500], mouse anti-NPHS2 (Proteintech, 20384-1-AP) [1:500], rabbit anti-podocin (Invitrogen, PA5-79757) [1:500], and streptavidin-HRP (Cell Signaling, 3999S) [1:1000] were applied in 3% BSA + TBST. The membrane and primary antibodies were allowed to incubate overnight at 4°C with gentle nutation. Following 3 min × 10 min washes with TBST, membranes were probed with secondary antibodies conjugated to horseradish peroxidase (HRP) (donkey- and rabbit-HRP [1:500] or goat anti-mouse-HRP [1:500] and incubated for 1 hour at room temperature. Membranes were developed with enhanced chemiluminescence substrate (ECL) and visualized on an iBright FL1000 (Invitrogen).

Proteomics data analysis

Raw data were processed using the MaxQuant software suite (version 1.6.12.0) for identification and label-free quantitation (Cox and Mann, 2008). Data were searched against a Uniprot Reviewed Mouse database (downloaded January 2021, containing 17,051 sequences) using the integrated Andromeda search engine. A maximum of two missed tryptic cleavages was allowed. The variable modification specified was oxidation of methionine, N-terminal acetylation, and phosphorylation of Ser/Thr/Tyr. Label-free quantitation (LFQ) was enabled. The results were filtered to 1% FDR at the unique peptide level and grouped into proteins within MaxQuant. Match between runs was enabled. Data were filtered in Perseus and then imported into Argonaut for normalization, imputation, and statistical analysis (Brademan et al., 2020). The analysis results are reported in Supplemental Excel files 1–3. We combined three separate MS analyses and averaged the log2 fold changes and respective *p*-values of the top 17 proteins identified across all three MS profiles. QIAGEN Ingenuity Pathway Analysis (IPA) was utilized to identify putative interactomes.

Immunofluorescence

Kidneys were harvested in cold filter-sterilized PBS and fixed at 4°C for 1 h in 4% paraformaldehyde (PFA) in PBS. The samples were washed twice in 1x PBS, placed in 30% sucrose overnight, and subsequently embedded in OCT. Kidneys were cut in 12-µm sections on a Leica Cryostat CM 1850. Tissue sections were blocked in 3% donkey serum, 1% BSA, 1x PBS, 0.1% Triton-X-100 for 45 min at room temperature. Slides were incubated in primary antibodies (see antibodies utilized as follows, Supplementary Table S6) diluted in blocking buffer for 1–2 h. The slides were then rinsed 3 min × 5 min in 1x PBST, after which they were incubated with Alexa Fluor-labeled secondary antibodies (Invitrogen) diluted (1:1000) in blocking buffer for 1 h at room temperature. The slides were then rinsed 2 min × 5 min with 1x PBST, 1 min × 3–5 min with 1x PBS +1 ng/mL DAPI, and mounted in ProLong Gold Antifade reagent (Invitrogen).

For double labeling tissues with two antibodies both raised in rabbit, we utilized a Zenon double labeling kit (Z25302, Invitrogen) with rabbit anti-Fnbp1l, rabbit anti-Ildr2, rabbit anti-podocin, and rabbit anti-HA antibodies. The weaker of the two primary rabbit antibodies, typically Ildr2 and Fnbp1l, was diluted in block solution and then incubated for 90 min at room temperature. The slides were washed 3–6x with 1x PBS +0.25% Triton-X 100 and subsequently incubated for 1 h at room temperature with the appropriate Alexa Fluor-488 labeled secondary antibody diluted 1:1000 in blocking buffer. The second primary rabbit antibody was mixed at a 1:

2.5 ratio with the Zenon fluorophore-647. It should be noted that the two fluorophores utilized are on opposite ends of the fluorescence spectrum. The slides were then fixed in 4% PFA for 5 min at room temperature. In addition, all subsequent steps were carried out per normal immunofluorescence procedures as mentioned previously. Images were acquired utilizing a Zeiss 880 confocal microscope equipped with Airyscan super-resolution and spectral imaging on Zen Microscopy Suite version 2.3 Sp1 that is part of the UNC Hooker Imaging Core. Z-stack images were acquired in 1 µm steps for Ildr2 and Fnbp1l.

Immunogold electron microscopy

Mouse kidneys were fixed for 1 h at room temperature in 4% PFA in 0.15 M sodium phosphate buffer pH 7.4 (PB) or 2% PFA +0.5% glutaraldehyde in 0.15 M PB and immediately processed for LR white resin embedding. The samples were washed in 0.15 M PB, 3 min × 10 min, and dehydrated using a PELCO BioWave Pro Microwave (Ted Pella, Inc.) as follows: at 40°C (750 W): 30% ethanol in water (ETOH) −1 min, 50% ETOH in water −1 min, 75% ETOH in water −1 min, and at 40°C (450 W): 100% ETOH −1 min, 100% ETOH −1 min, 100% ETOH −1 min. Microwave infiltration and embedment were carried out using the following process: 1 part 100% ETOH: 2 part LR white resin −10 min at 40°C (350 W), two exchanges of 100% LR white resin for 10 min at 50°C (350 W). The samples were transferred to 00 gelatin capsules filled with fresh LR white resin and polymerized overnight at 55°C. The temperature was adjusted to 60°C for 6 h and allowed to completely polymerize at room temperature for 72 h. Blocks were trimmed to the tissue, and 1.0-µm sections were cut using Leica Ultracut UCT (Leica Microsystems, Inc.) and a Diatome diamond knife (Electron Microscopy Sciences). The sections were mounted on glass slides, stained with 1% toluidine blue O in 1% sodium borate, and regions with glomeruli were selected and trimmed (Reynolds, 1963). Ultrathin sections (90 nm) were cut and mounted on formvar-/carbon-coated 200-mesh nickel grids. Before immunostaining, the sections were hydrated by floating the grids section-side down on drops of deionized water. The sections were blocked with AURION Goat Blocking Solution for 15 min and transferred to 15 µL drops of the primary antisera diluted at [1: 500] for anti-HA and [1: 250] for anti-podocin in 0.05 M TBS+ 0.2% BSA-Ac, pH 7.6 (rabbit anti-HA, Cell Signaling, 37245; rabbit anti-podocin, Invitrogen, PA5-79757). The sections were incubated overnight at 4°C followed by 4 min × 10 min washes in TBS/BSA-Ac to remove the unbound antibody. The grids were incubated in a 12 nm Colloidal Gold-AffiniPure goat anti-rabbit IgG (H + L) secondary antibody (Jackson Immuno, Lot #148041) diluted at 1:50 in TBS/BSA-Ac for 2 h at room temperature (Hobot and Newman, 1996). After three washes in TBS/BSA-Ac and three washes in 0.15 M PB, the grids were post-fixed for 10 min in 1% glutaraldehyde in 0.15 M PB followed by three washes in deionized water. The grids were stained with 4% aqueous uranyl acetate for 5 min for additional contrast. The samples were observed using a JEOL JEM-1230 transmission electron microscope operating at 80 kV (JEOL United States INC.), and images were taken using a Gatan Orius SC1000 CCD camera with Gatan Microscopy Suite version 3.10.1002.0 software (Gatan, Inc.). Sample preparation and imaging were performed at the UNC Microscopy Services Laboratory, Department of Pathology and Laboratory Medicine.

In situ hybridization

Wild-type C57/Bl6J kidneys at postnatal day 2 (P2) were dissected in cold molecular-grade PBS (RNAse-/DNAse-free) and fixed in 4% PFA for 30 min at room temperature on a rocking platform. The kidneys were washed in molecular-grade PBS and placed in 30% sucrose. The kidneys were embedded in OCT, and 20-µm sections were cut on a cryostat (Leica CM 1850). Tissue sections were fixed in 4% PFA and washed with 1x PBS. The tissue was permeabilized with proteinase K at 10 µg/mL for 15 min and subsequently washed with 1x PBS. The tissue was then washed in an acetylation solution (0.1% HCl, 0.375% acetic anhydride, and 0.75% triethanolamine in H_20) for 10 min with stirring. The tissue sections were then subsequently washed for 3 min × 3 min with PBS, rinsed for 1 min × 5 min in 0.85% NaCl, 1 min × 5 min in 70% ethanol, and 1 min × 5 min in 95% ethanol prior to riboprobe/hybridization application. Antisense digoxygenin (DIG)-labeled riboprobes were hybridized to the tissue in a solution containing 50% deionized formamide, two sodium citrate pH 4.5, 1% SDS, 50 µg/mL heparin, and 50 µg/mL yeast tRNA overnight in a humidity chamber at 68°C. The following day, the specimens were treated with successive washes of sodium citrate buffer as described previously (Liu et al., 2017) and blocked in 10% heat-inactivated sheep serum (HISS), with 2% Roche blocking reagent (BR) in malic acid-buffered solution with 0.1% Tween-20 (MABT). Anti-DIG-alkaline phosphatase (AP) antibody was applied in 1% HISS, 2% BR in MABT overnight at 4°C. The following day, the slides were washed in MABT and 100 mM NaCl, 100 mM Tris-HCl pH 9.5, 50 mM $MgCl_2$, and 0.1% Tween-20 (NTMT) with 2 mM levamisole to inhibit endogenous alkaline phosphatase activity. Digoxigenin-UTP (Roche 53119620)-labeled riboprobes were amplified from cDNA libraries collected from the mouse kidney tissue with the following primers:

Podocin forward primer: TGACGTTCCCTTTTTCCATC, podocin reverse primer with T7 underlined: CAGTGAATTGTA ATACGACTCACTATAGGGCTGTGGACAGCGACTGAAGA.

Ildr2 forward: GGAGAATCCTTGGGC and Ildr2 reverse: CAG TGAATTGTAATACGACTCACTATAGGGGTACCCGGCCTTGGC were previously published (Liu et al., 2017). Fnbp1l forward primer: GCTGAATGACAATTGTGTGAAC and Fnbp1l reverse: CAGTGA ATTGTAATACGACTCACTATAGGGCTGTGCAAGTCCAAGTGT CTTC.

Human kidney tissue

Human kidney tissue samples were de-identified (young) or directly donated (91-year-old) and did not necessitate IRB approval. Young, normal kidney tissue was obtained from the UNC Tissue Procurement Facility as a frozen block. A small piece of tissue was removed with a razor blade, fixed for 10 min in 4% paraformaldehyde, and subsequent processing for cryosectioning and immunofluorescence was carried out as for the mouse (described previously). For the old kidney tissue, a fresh sample was excised from the kidney cortex and fixed for 10 min in 4% paraformaldehyde prior to processing, similar to the young tissue, for immunofluorescence.

Data availability statement

The mass spectrometry proteomics data have been deposited to the ProteomeXchange Consortium (http://www.proteomexchange.org/) via the PRIDE partner repository (https://www.ebi.ac.uk/pride/) with the dataset identifier PXD042301.

Ethics statement

The animal study was reviewed and approved by IACUC 19-183.0/22-136.0.

Author contributions

GG helped design the study, performed the experiments, and wrote the manuscript. ZI, SC, and AS helped perform the experiments. LO'B conceptualized the podocin–BioID model, designed and oversaw the study, and edited the manuscript. All authors contributed to the article and approved the submitted version.

Funding

This research is based, in part, on work conducted at the Microscopy Services Laboratory (TEM), the UNC Proteomics Core Facility (MS), and the UNC Hooker Imaging Core Facility (confocal microscopy), which are supported, in part, by P30CA016086 Cancer Center Core Support Grant to the UNC Lineberger Comprehensive Cancer Center. This research was supported, in part, by a Vanderbilt O'Brien Kidney Center Pilot and Feasibility Award (P30DK114809), a UNC Junior Faculty Development Award, and Start-Up funds from UNC to LO'B, as well as from F32AR073649 and L40DK130217 to GG.

Acknowledgments

The authors would like to acknowledge the many people and core services at the University of North Carolina at Chapel Hill who aided in this investigation. The authors specifically would like to thank Wendy Salmon, Director of the Department of Cell Biology and Physiology's Hooker Imaging Core, Laura Herring, Ph.D., Director of the School of Medicine's Michael Hooker Proteomics Center, Victoria Madden and Kristen White, providers of electron microscopy services in the Department of Pathology and Laboratory Medicine's Microscopy Services Laboratory, and Paul Risteff for training in TEM and aid with image acquisition and sample preparation. The authors would further like to acknowledge the members of the O'Brien lab for critical feedback on these studies.

Conflict of interest

The authors declare that the research was conducted in the absence of any commercial or financial relationships that could be construed as a potential conflict of interest.

Publisher's note

All claims expressed in this article are solely those of the authors and do not necessarily represent those of their affiliated organizations, or those of the publisher, the editors, and the reviewers. Any product that may be evaluated in this article, or claim that may be made by its manufacturer, is not guaranteed or endorsed by the publisher.

Supplementary material

The Supplementary Material for this article can be found online at: https://www.frontiersin.org/articles/10.3389/fcell.2023.1195037/full#supplementary-material

References

Asanuma, K., Campbell, K. N., Kim, K., Faul, C., and Mundel, P. (2007). Nuclear relocation of the nephrin and cd2ap-binding protein dendrin promotes apoptosis of podocytes. *Proc. Natl. Acad. Sci. U.S.A.* 104 (24), 10134–10139. doi:10.1073/pnas.0700917104

Beltcheva, O., Martin, P., Lenkkeri, U., and Tryggvason, K. (2001). Mutation spectrum in the nephrin gene (NPHS1) in congenital nephrotic syndrome. *Hum. Mutat.* 17 (5), 368–373. doi:10.1002/humu.1111

Bierzynska, A., Soderquest, K., Dean, P., Colby, E., Rollason, R., Jones, C., et al. (2017). *MAGI2* mutations cause congenital nephrotic syndrome. *J. Am. Soc. Nephrol.* 28 (5), 1614–1621. doi:10.1681/ASN.2016040387

Boerries, M., Grahammer, F., Eiselein, S., Buck, M., Meyer, C., Goedel, M., et al. (2013). Molecular fingerprinting of the podocyte reveals novel gene and protein regulatory networks. *Kidney Int.* 83 (6), 1052–1064. doi:10.1038/ki.2012.487

Boute, N., Gribouval, O., Roselli, S., Benessy, F., Lee, H., Fuchshuber, A., et al. (2000). NPHS2, encoding the glomerular protein podocin, is mutated in autosomal recessive steroid-resistant nephrotic syndrome. *Nat. Genet.* 24 (4), 349–354. doi:10.1038/74166

Brademan, D. R., Miller, I. J., Kwiecien, N. W., Pagliarini, D. J., Westphall, M. S., Coon, J. J., et al. (2020). Argonaut: A web platform for collaborative multi-omic data visualization and exploration. *Patterns* 1 (7), 100122. doi:10.1016/j.patter.2020.100122

Branon, T. C., Bosch, J. A., Sanchez, A. D., Udeshi, N. D., Svinkina, T., Carr, S. A., et al. (2018). Efficient proximity labeling in living cells and organisms with TurboID. *Nat. Biotechnol.* 36 (9), 880–887. doi:10.1038/nbt.4201

Cox, J., and Mann, M. (2008). MaxQuant enables high peptide identification rates, individualized p.p.b.-range mass accuracies and proteome-wide protein quantification. *Nat. Biotechnol.* 26 (12), 1367–1372. doi:10.1038/nbt.1511

D'Agati, V. (2003). Pathologic classification of focal segmental glomerulosclerosis. *Seminars Nephrol.* 23 (2), 117–134. doi:10.1053/snep.2003.50012

Diez-Roux, G., Banfi, S., Sultan, M., Geffers, L., Anand, S., Rozado, D., et al. (2011). A high-resolution anatomical atlas of the transcriptome in the mouse embryo. *PLoS Biol.* 9 (1), e1000582. doi:10.1371/journal.pbio.1000582

Donoviel, D. B., Freed, D. D., Vogel, H., Potter, D. G., Hawkins, E., Barrish, J. P., et al. (2001). Proteinuria and perinatal lethality in mice lacking NEPH1, a novel protein with homology to NEPHRIN. *Mol. Cell Biol.* 21 (14), 4829–4836. doi:10.1128/MCB.21.14.4829-4836.2001

Ebnet, K., Suzuki, A., Ohno, S., and Vestweber, D. (2004). Junctional adhesion molecules (JAMs): More molecules with dual functions? *J. Cell Sci.* 117 (1), 19–29. doi:10.1242/jcs.00930

Ettou, S., Jung, Y. L., Miyoshi, T., Jain, D., Hiratsuka, K., Schumacher, V., et al. (2020). Epigenetic transcriptional reprogramming by WT1 mediates a repair response during podocyte injury. *Sci. Adv.* 6 (30), eabb5460. eabb5460. doi:10.1126/sciadv.abb5460

Firat-Karalar, E. N., Rauniyar, N., Yates, J. R., and Stearns, T. (2014). Proximity interactions among centrosome components identify regulators of centriole duplication. *Curr. Biol.* 24 (6), 664–670. doi:10.1016/j.cub.2014.01.067

Fukasawa, H., Bornheimer, S., Kudlicka, K., and Farquhar, M. G. (2009). Slit diaphragms contain tight junction proteins. *J. Am. Soc. Nephrol.* 20 (7), 1491–1503. doi:10.1681/ASN.2008101117

Gerlach, G. F., and Wingert, R. A. (2014). Zebrafish pronephros tubulogenesis and epithelial identity maintenance are reliant on the polarity proteins prkc iota and zeta. *Dev. Biol.* 396 (2), 183–200. doi:10.1016/j.ydbio.2014.08.038

Gigante, M., Pontrelli, P., Montemurno, E., Roca, L., Aucella, F., Penza, R., et al. (2009). CD2AP mutations are associated with sporadic nephrotic syndrome and focal segmental glomerulosclerosis (FSGS). *Nephrol. Dial. Transplant.* 24 (6), 1858–1864. doi:10.1093/ndt/gfn712

Go, C. D., Knight, J. D. R., Rajasekharan, A., Rathod, B., Hesketh, G. G., Abe, K. T., et al. (2021). A proximity-dependent biotinylation map of a human cell. *Nature* 595 (7865), 120–124. doi:10.1038/s41586-021-03592-2

Guaragna, M. S., Lutaif, A. C. G. B., Piveta, C. S. C., Souza, M. L., de Souza, S. R., Henriques, T. B., et al. (2015). NPHS2 mutations account for only 15% of nephrotic syndrome cases. *BMC Med. Genet.* 16, 88. doi:10.1186/s12881-015-0231-9

Hecht, I., Toporik, A., Podojil, J. R., Vaknin, I., Cojocaru, G., Oren, A., et al. (2018). ILDR2 is a novel B7-like protein that negatively regulates T cell responses. *J. Immunol.* 200 (6), 2025–2037. doi:10.4049/jimmunol.1700325

Higashi, T., Tokuda, S., Kitajiri, S., Masuda, S., Nakamura, H., Oda, Y., et al. (2013). Analysis of the "angulin" proteins LSR, ILDR1 and ILDR2-tricellulin recruitment, epithelial barrier function and implication in deafness pathogenesis. *J. Cell Sci.* 126 (4), 966–977. doi:10.1242/jcs.116442

Ho, H.-Y. H., Rohatgi, R., Lebensohn, A. M., Le MaLi, J., Gygi, S. P., et al. (2004). Toca-1 mediates cdc42-dependent actin nucleation by activating the N-WASP-WIP complex. *Cell* 118 (2), 203–216. doi:10.1016/j.cell.2004.06.027

Hobot, J. A., and Newman, G. R. (1996). Immunomicroscopy: Resin techniques and on-section labelling with immunocolloidal gold or immunoperoxidase-planning a protocol. *Scanning Microsc.* 10 (1), 121–143.

Huber, T. B., Kottgen, M., Schilling, B., Walz, G., and Benzing, T. (2001). Interaction with podocin facilitates nephrin signaling. *J. Biol. Chem.* 276 (45), 41543–41546. doi:10.1074/jbc.C100452200

Huetter, J., Gritzan, U., Gutcher, I., Doecke, W.-D., Luetke-Eversloh, M. V., Golfier, S., et al. (2020). Characterization of BAY 1905254, an immune checkpoint inhibitor targeting the immunoglobulin-like domain containing receptor 2 (ILDR2). *Cancer Immunol. Res.* 8 (7), 895–911. doi:10.1158/2326-6066.CIR-19-0321

Ichimura, K., Kakuta, S., Kawasaki, Y., Miyaki, T., Nonami, T., Miyazaki, N., et al. (2017). Morphological process of podocyte development revealed by block-face scanning electron microscopy. *J. Cell Sci.* 130 (1), 132–142. doi:10.1242/jcs.187815

Ichimura, K., Miyazaki, N., Sadayama, S., Murata, K., Koike, M., Nakamura, K., et al. (2015). Three-dimensional architecture of podocytes revealed by block-face scanning electron microscopy. *Sci. Rep.* 5 (1), 8993. doi:10.1038/srep08993

Karnovsky, M., and Ryan, G. (1975). Substructure of the glomerular slit diaphragm in freeze-fractured normal rat kidney. *J. Cell Biol.* 65 (1), 233–236. doi:10.1083/jcb.65.1.233

Kestilä, M., Lenkkeri, U., Männikkö, M., Lamerdin, J., McCready, P., Putaala, H., et al. (1998). Positionally cloned gene for a novel glomerular protein-nephrin-is mutated in congenital nephrotic syndrome. *Mol. Cell* 1 (4), 575–582. doi:10.1016/s1097-2765(00)80057-x

Kim, D. I., Jensen, S. C., Noble, K. A., Kc, B., Roux, K. H., Motamedchaboki, K., et al. (2016). An improved smaller biotin ligase for BioID proximity labeling. *Mol. Biol. Cell* 27 (8), 1188–1196. doi:10.1091/mbc.E15-12-0844

Kocylowski, M. K., Aypek, H., Bildl, W., Helmstädter, M., Trachte, P., Dumoulin, B., et al. (2022). A slit-diaphragm-associated protein network for dynamic control of renal filtration. *Nat. Commun.* 13 (1), 6446. doi:10.1038/s41467-022-33748-1

Kopp, J. B., Anders, H.-J., Susztak, K., Podestà, M. A., Remuzzi, G., Hildebrandt, F., et al. (2020). *Podocytopathies.* Nat. Rev. Dis. Prim. 6 (1), 68. doi:10.1038/s41572-020-0196-7

Liu, Y.-X., Zhang, A.-Q., Luo, F.-M., Sheng, Y., Wang, C.-Y., Dong, Y., et al. (2021). Case report: A novel heterozygous mutation of CD2AP in a Chinese family with proteinuria leads to focal segmental glomerulosclerosis. *Front. Pediatr.* 9, 687455. doi:10.3389/fped.2021.687455

Liu, Y., Nie, H., Liu, C., Zhai, X., Sang, Q., Wang, Y., et al. (2017). Angulin proteins ILDR1 and ILDR2 regulate alternative pre-MRNA splicing through binding to splicing factors TRA2A, TRA2B, or SRSF1. *Sci. Rep.* 7 (1), 7466. doi:10.1038/s41598-017-07530-z

Lu, C.-C., Wang, G.-H., Lu, J., Chen, P.-P., Zhang, Y., Hu, Z.-B., et al. (2019). "Role of podocyte injury in glomerulosclerosis," in *Renal fibrosis: Mechanisms and therapies*. Editors B.-C. Liu, H.-Y. Lan, and L.-L. Lv (Singapore: Springer), 195–232. doi:10.1007/978-981-13-8871-2_10

Lu, Y., Ye, Y., Bao, W., Yang, Q., Wang, J., Liu, Z., et al. (2017). Genome-wide identification of genes essential for podocyte cytoskeletons based on single-cell RNA sequencing. *Kidney Int.* 92 (5), 1119–1129. doi:10.1016/j.kint.2017.04.022

May, D. G., Scott, K. L., Campos, A. R., and Roux, K. J. (2020). Comparative application of BioID and TurboID for protein-proximity biotinylation. *Cells* 9 (5), 1070. doi:10.3390/cells9051070

McKee, R., Gerlach, G. F., Jou, J., Cheng, C. N., and Wingert, R. A. (2014). Temporal and spatial expression of tight junction genes during zebrafish pronephros development. *Gene Expr. Patterns* 16 (2), 104–113. doi:10.1016/j.gep.2014.11.001

Mick, D. U., Rodrigues, R. B., Leib, R. D., Adams, C. M., Chien, A. S., Gygi, S. P., et al. (2015). Proteomics of primary cilia by proximity labeling. *Dev. Cell* 35 (4), 497–512. doi:10.1016/j.devcel.2015.10.015

Miyaki, T., Kawasaki, Y., Hosoyamada, Y., Amari, T., Kinoshita, M., Matsuda, H., et al. (2020). Three-dimensional imaging of podocyte ultrastructure using FE-SEM and FIB-sem tomography. *Cell Tissue Res.* 379 (2), 245–254. doi:10.1007/s00441-019-03118-3

Pagtalunan, M. E., Miller, P. L., Jumping-Eagle, S., Nelson, R. G., Myers, B. D., Rennke, H. G., et al. (1997). Podocyte loss and progressive glomerular injury in type II diabetes. *J. Clin. Invest.* 99 (2), 342–348. doi:10.1172/JCI119163

Pieperhoff, S., Rickelt, S., Heid, H., Claycomb, W. C., Zimbelmann, R., Kuhn, C., et al. (2012). The plaque protein Myozap identified as a novel major component of adhering junctions in endothelia of the blood and the lymph vascular systems. *J. Cell. Mol. Med.* 16 (8), 1709–1719. doi:10.1111/j.1582-4934.2011.01463.x

Pierchala, B. A., Muñoz, M. R., and Tsui, C. C. (2010). Proteomic analysis of the slit diaphragm complex: CLIC5 is a protein critical for podocyte morphology and function. *Kidney Int.* 78 (9), 868–882. doi:10.1038/ki.2010.212

Podojil, J. R., Hecht, I., Chiang, M.-Y., Vaknin, I., Barbiro, I., Novik, A., et al. (2018). ILDR2-Fc is a novel regulator of immune homeostasis and inducer of antigen-specific immune tolerance. *J. Immunol.* 200 (6), 2013–2024. doi:10.4049/jimmunol.1700326

Quaggin, S. E., and Kreidberg, J. A. (2008). Development of the renal glomerulus: Good neighbors and good fences. *Development* 135 (4), 609–620. doi:10.1242/dev.001081

Reeves, W., Caulfield, J. P., and Farquhar, M. G. (1978). Differentiation of epithelial foot processes and filtration slits: Sequential appearance of occluding junctions, epithelial polyanion, and slit membranes in developing glomeruli. *Lab. Invest.* 39 (2), 90–100.

Reiser, J., Kriz, W., Kretzler, M., and Mundel, P. (2000). The glomerular slit diaphragm is a modified adherens junction. *J. Am. Soc. Nephrol.* 11 (1), 1–8. doi:10.1681/ASN.V1111

Reynolds, E. S. (1963). The use of lead citrate at high Ph as an electron-opaque stain in electron microscopy. *J. Cell Biol.* 17 (1), 208–212. doi:10.1083/jcb.17.1.208

Rinschen, M. M., Gödel, M., Grahammer, F., Zschiedrich, S., Helmstädter, M., Kretz, O., et al. (2018). A multi-layered quantitative *in vivo* expression atlas of the podocyte unravels kidney disease candidate genes. *Cell Rep.* 23 (8), 2495–2508. doi:10.1016/j.celrep.2018.04.059

Rodewald, R., and Karnovsky, M. J. (1974). Porous substructure of the glomerular slit diaphragm in the rat and mouse. *J. Cell Biol.* 60 (2), 423–433. doi:10.1083/jcb.60.2.423

Roselli, S., Gribouval, O., Boute, N., Sich, M., Benessy, F., Attié, T., et al. (2002). Podocin localizes in the kidney to the slit diaphragm area. *Am. J. Pathology* 160 (1), 131–139. doi:10.1016/S0002-9440(10)64357-X

Roselli, S., Heidet, L., Sich, M., Henger, A., Kretzler, M., Gubler, M.-C., et al. (2004). Early glomerular filtration defect and severe renal disease in podocin-deficient mice. *Mol. Cell. Biol.* 24 (2), 550–560. doi:10.1128/MCB.24.2.550-560.2004

Roux, K. J., Kim, D. I., Raida, M., and Burke, B. (2012). A promiscuous biotin ligase fusion protein identifies proximal and interacting proteins in mammalian cells. *J. Cell Biol.* 196 (6), 801–810. doi:10.1083/jcb.201112098

Rudolph, F., Fink, C., Hüttemeister, J., Kirchner, M., Radke, M. H., Lopez Carballo, J., et al. (2020). Deconstructing sarcomeric structure–function relations in titin-BioID knock-in mice. *Nat. Commun.* 11 (1), 3133. doi:10.1038/s41467-020-16929-8

Schurek, E.-M., Völker, L. A., Tax, J., Lamkemeyer, T., Rinschen, M. M., Ungrue, D., et al. (2014). A disease-causing mutation illuminates the protein membrane topology of the kidney-expressed prohibitin homology (PHB) domain protein podocin. *J. Biol. Chem.* 289 (16), 11262–11271. doi:10.1074/jbc.M113.521773

Schwarz, K., Simons, M., Reiser, J., Saleem, M. A., Faul, C., Kriz, W., et al. (2001). Podocin, a raft-associated component of the glomerular slit diaphragm, interacts with CD2AP and nephrin. *J. Clin. Invest.* 108 (11), 1621–1629. doi:10.1172/JCI12849

Sears, R. M., May, D. G., and Roux, K. J. (2019). BioID as a tool for protein-proximity labeling in living cells. *Methods Mol. Biol.* 2012, 299–313. doi:10.1007/978-1-4939-9546-2_15

Seeger, T. S., Frank, D., Rohr, C., Will, R., Just, S., Grund, C., et al. (2010). Myozap, a novel intercalated Disc protein, activates serum response factor-dependent signaling and is required to maintain cardiac function *in vivo*. *Circ. Res.* 106 (5), 880–890. doi:10.1161/CIRCRESAHA.109.213256

Sellin, L., Huber, T. B., Gerke, P., Quack, I., Pavenstädt, H., and Walz, G. (2003). NEPH1 defines a novel family of podocin interacting proteins. *FASEB J.* 17 (1), 115–117. doi:10.1096/fj.02-0242fje

Thisse, B., and Thisse, C. (2004). "Fast release clones: A high throughput expression analysis," (Berlin, Germany: ScienceOpen, Inc). Thesis.

Uezu, A., Kanak, D. J., Bradshaw, T. W. A., Soderblom, E. J., Catavero, C. M., Burette, A. C., et al. (2016). Identification of an elaborate complex mediating postsynaptic inhibition. *Science* 353 (6304), 1123–1129. doi:10.1126/science.aag0821

van den berg, J. G., van den Bergh Weerman, M. A., Assmann, K. J. M., Weening, J. J., and Florquin, S. (2004). Podocyte foot process effacement is not correlated with the level of proteinuria in human glomerulopathies. *Kidney Int.* 66 (5), 1901–1906. doi:10.1111/j.1523-1755.2004.00964.x

Van Itallie, C. M., Tietgens, A. J., Krystofiak, E., Kachar, B., and Anderson, J. M. (2015). A complex of ZO-1 and the BAR-domain protein TOCA-1 regulates actin assembly at the tight junction. *MBoC* 26 (15), 2769–2787. doi:10.1091/mbc.E15-04-0232

Wang, Y., Eng, D. G., Kaverina, N. V., Loretz, C. J., Koirala, A., Akilesh, S., et al. (2020). Global transcriptomic changes occur in aged mouse podocytes. *Kidney Int.* 98 (5), 1160–1173. doi:10.1016/j.kint.2020.05.052

Wu, H., Kirita, Y., Donnelly, E. L., and Humphreys, B. D. (2019). Advantages of single-nucleus over single-cell RNA sequencing of adult kidney: Rare cell types and novel cell states revealed in fibrosis. *J. Am. Soc. Nephrol.* 30 (1), 23–32. doi:10.1681/ASN.2018090912

Wu, H., Malone, A. F., Donnelly, E. L., Kirita, Y., Uchimura, K., Ramakrishnan, S. M., et al. (2018). Single-cell Transcriptomics of a human kidney allograft biopsy specimen defines a diverse inflammatory response. *J. Am. Soc. Nephrol.* 29 (8), 2069–2080. doi:10.1681/ASN.2018020125

Yu, H. H., and Zallen, J. A. (2020). Abl and canoe/afadin mediate mechanotransduction at tricellular junctions. *Science* 370 (6520), eaba5528. eaba5528. doi:10.1126/science.aba5528